The Astronomical Journal, 144:79 (22pp), 2012 September doi:10.1088/0004-6256/144/3/79


# OPTICAL AND X-RAY OBSERVATIONS OF THE MERGING CLUSTER AS1063

P. L. Gómez[1], L. E. Valkonen[2], A. K. Romer[2], E. Lloyd-Davies[2], T. Verdugo[3], C. M. Cantalupo[4], M. D. Daub[5], J. H. Goldstein[6,7], C. L. Kuo[8,9], A. E. Lange[8,10], M. Lueker[5], W. L. Holzapfel[5], J. B. Peterson[11], J. Ruhl[2], M. C. Runyan[8], C. L. Reichardt[5], and K. Sabirli[2,11]

[1] Gemini Observatory, Southern Operations Center, c/o AURA, Casilla 603, La Serena, Chile
[2] Astronomy Centre, Department of Physics & Astronomy, University of Sussex, Falmer, Brighton, BN1 9QH, UK
[3] Departamento de Física y Astronomia, Universidad de Valparaíso, Avenida Gran Bretaña 1111, Valparaíso, Chile
[4] Lawrence Berkeley National Lab, 1 Cyclotron Road Mail Stop 50F, Berkeley, CA 94720-8139, USA
[5] Department of Physics, University of California, Berkeley, CA 94720, USA
[6] Department of Physics, Case Western Reserve University, Cleveland, OH 44106, USA
[7] Arreté Associates, Arlington, VA 22202, USA
[8] Observational Cosmology, California Institute of Technology, MS 59-33, Pasadena, CA 91125, USA
[9] Department of Physics and KIPAC, Stanford University, Stanford, CA 94305, USA
[10] Jet Propulsion Laboratory, 4800 Oak Grove Drive, Pasadena, CA 91109, USA
[11] Department of Physics, Carnegie Mellon University, Pittsburgh, PA 15213, USA
*Received 2012 April 12; accepted 2012 June 28; published 2012 August 9*

## ABSTRACT

We present the first in-depth analysis of the massive cluster AS1063. This is one of the hottest X-ray clusters discovered to date and is undergoing a major merging event. The average temperature of the hot intracluster medium has been measured, using *Chandra*/ACIS-I, and found to be >11.5 keV. Optical spectroscopy, from GMOS-S, has provided a mean redshift of 0.3461 and a large velocity dispersion of $1840^{+230}_{-150}$ km s$^{-1}$. Both the large velocity dispersion and high X-ray temperature suggest a very massive cluster ($M_{200} > 2.5 \times 10^{15}\, M_{\odot}$) and/or a merger system. The merger model is supported by a small offset between the galaxy density and the peak of the X-ray emission, the presence of offset and twisted X-ray isophotes, and a non-Gaussian galaxy velocity distribution. We also report that the velocity distribution is better represented by the velocity dispersion produced during a merger than by the velocity distribution of a relaxed cluster. Moreover, we find that two non-concentric beta models are a better description for the distribution of the cluster gas than a single beta model. Therefore, we propose that a recent merger event close to the plane of the sky is responsible for the observed properties of the cluster. In addition, optical imaging, from SuSI2 on the New Technology Telescope and GMOS-S at Gemini, has also uncovered the presence of several gravitational arcs that have been used to further constrain the mass and dynamics of the cluster.

*Key word:* galaxies: clusters: general

## 1. INTRODUCTION

The study of the most massive clusters of galaxies is very important because it allows us to gain a better understanding of how clusters grow and evolve. The advantage of studying the most massive systems is that they are assembled within very deep gravitational potential wells and therefore have significant weak and strong lensing signals. Moreover, these deep gravitational potential wells contain dense intracluster gas that can be easily detected by its bright X-ray emission and strong Sunyaev–Zel'dovich effect (Sunyaev & Zel'dovich 1970) signatures. The combination of high-quality observations with numerical simulations of cluster evolution has explained several physical processes present in galaxy clusters and uncovered new ways to use them as robust cosmological probes (e.g., Nagai et al. 2007). For instance, these studies have helped us to understand how shocks and cold fronts appear as the observable signatures of major mergers (e.g., Markevitch & Vikhlinin 2007). In order to improve our knowledge of cluster mergers (i.e., physical properties and their observable signatures) it is important to study in detail even more examples of mergers of all types and at all stages of evolution.

AS1063 (Abell et al. 1989) is a massive cluster that has not been studied in detail before. This is surprising because it is the second most luminous cluster in the *ROSAT*-ESO Flux Limited X-ray (Böhringer et al. 2004) Galaxy Cluster Survey, with a reported luminosity of $\sim 3.08 \times 10^{45}$ erg s$^{-1}$ in the rest frame 0.1–2.4 keV band. Indeed, until recently, there has been uncertainty about the redshift of the cluster: Abell et al. (1989) estimated a redshift for the cluster of $z = 0.252$, whereas Cruddace et al. (2002) reported $z = 0.1495$, based on the measurement of one galaxy, and Böhringer et al. (2004) published a value of $z = 0.348$, based on the measurement of three galaxies. The only pointed X-ray observation of this cluster is that described herein. Although these *Chandra* data have been presented before (Maughan et al. 2008), that analysis assumed an erroneous cluster redshift of 0.252. In this paper, we report our new optical data and a new X-ray data reduction, based on the correct cluster redshift. Both data sets reveal that this bright X-ray cluster is undergoing a merger event. We expect that these new data will help improve the understanding of the process of cluster merging.

In Sections 2 and 3, we report, respectively, our optical and X-ray observations and their data analysis. Our interpretations are discussed in Section 4. Finally, we summarize our findings in Section 5. Note that we use $H_0 = 75$ km s$^{-1}$ Mpc$^{-1}$, $\Omega_{\Lambda} = 0.7$, and a flat universe throughout the paper, so that $1' \simeq 270$ kpc. All errors are quoted to the $1\sigma$ level.

## 2. OPTICAL OBSERVATIONS

In this section, we report the optical observations of AS1063. We start by describing the imaging data obtained by the Gemini-South and ESO NTT telescopes and end

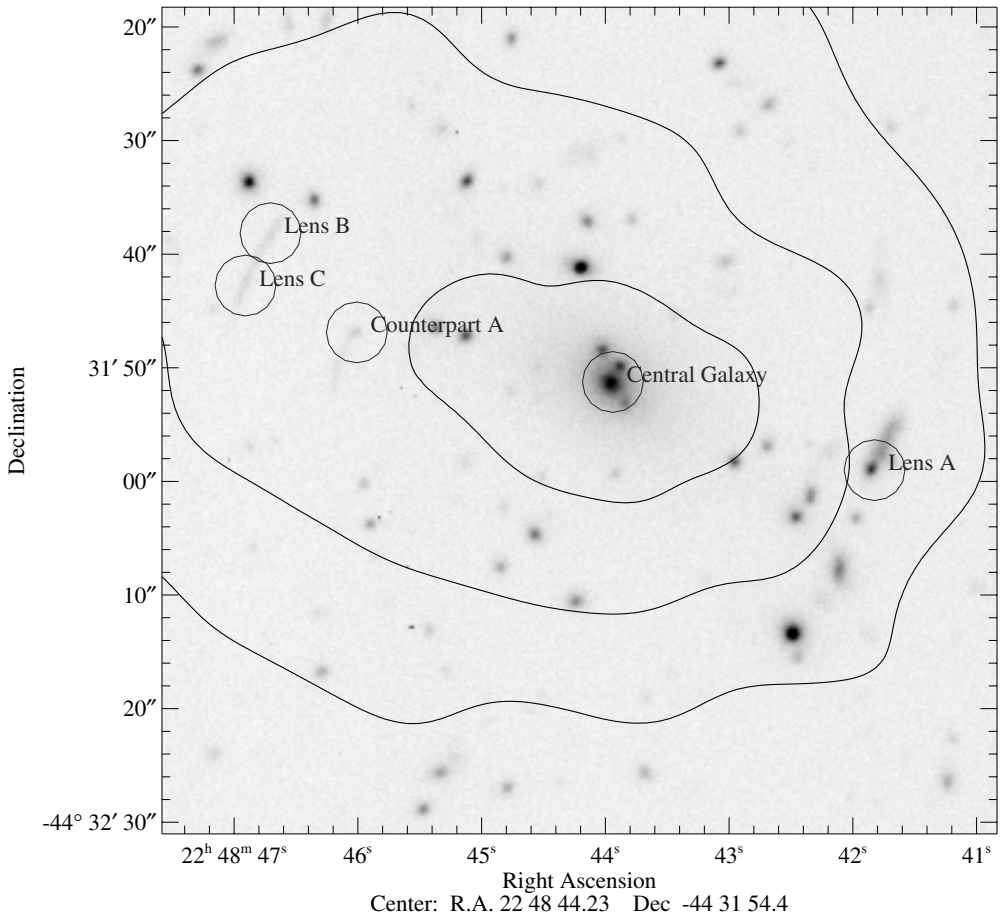


**Figure 1.** This is a grayscale SuSI2 image of the core of AS1063 in the *I* band. In this figure we have labeled the central galaxy and the candidate gravitational lenses. We have also identified a faint object labeled "Counterpart A" that seems to be another lensed image of object A. The contours are from the *Chandra* X-ray image.

with a description of the Gemini-South spectroscopic observations.

### 2.1. Optical Imaging

The imaging data consist of archival ESO NTT data and our own Gemini-South queue observations. The New Technology Telescope (NTT) imaging data were obtained using the Superb-Seeing Imager (SuSI2; D'Odorico et al. 1998) in 2002 October and consist of three 400 s *V*-band (∼0.7 arcsec seeing) and three 240 s *R*-band images (∼0.65 arcsec seeing). We reduced the individual SuSI2 images using the biases and sky twilights available from the archive. Next, we mosaicked the observations by co-adding the images into final *V*- and *R*-band images. These co-added images revealed the presence of several previously unknown gravitational arc candidates (Figure 1).

We also used the Gemini Multi-Object Spectrograph (GMOS; Hook et al. 2004) instrument to obtain eight $i'$-band images (200 s each) and eight $r'$-band images (225 s each) with small positional offsets between the frames. The observations were carried out in queue mode (program GS-2003B-Q-24) with an overall seeing of ∼0.9 arcsec and thin cirrus on the sky. The images were bias subtracted and flat fielded with sky twilight flats. In addition, the $i'$-band data were fringe corrected by subtracting a fringe frame from the images. Next, the GMOS images were mosaicked and co-added into final $r'$- and $i'$-band images. We identified and measured galaxy properties using the SExtractor program (Bertin & Arnouts 1996). We adopted the MAG-BEST estimate as the measurement of the galaxy magnitude. Even though the observations were not obtained under photometric conditions, we converted the observed counts into approximate magnitudes using the zero-point filter values listed on the Gemini public Web sites. We are aware that the absolute magnitudes could be off by up to ∼0.3 mag; however, the red sequence galaxies will still be easily identified in the color–magnitude diagram (see below and Figure 2). We combined the SExtractor output from the $r'$ and $i'$ images to construct a color–magnitude diagram. Figure 2 shows the color–magnitude diagram and Figure 3 shows the distribution on the sky of 711 objects derived from the SExtractor output. All of these objects are likely to be galaxies as they had the CLASS-STAR $< 0.8$. We selected a subsample of 329 of these 711 as candidate cluster members based on their position on the color–magnitude diagram (i.e., $0.0 < r' - i' < 0.8$, and $m_{r'} > 24.5$). This color cut includes most of the galaxies in the red sequence.

### 2.2. Optical Spectroscopy

From a total of 711 GMOS detected galaxies, 329 were selected as candidate cluster members based on their location on the color–magnitude diagram. In order to obtain GMOS-S spectroscopy of as many of these 329 as possible, we designed four multiobject masks. In total, we were able to put slits on only 116 galaxies due to the available 5′ field of view. Of these, 78 of the objects were drawn from the candidate cluster member list of 329 objects (see above). Another 35 were other galaxies drawn from the total list of 711 GMOS-detected objects. The remaining three galaxies were selected from the SuSI2 images as candidate lensed background galaxies (see Figure 1). The tilt and length

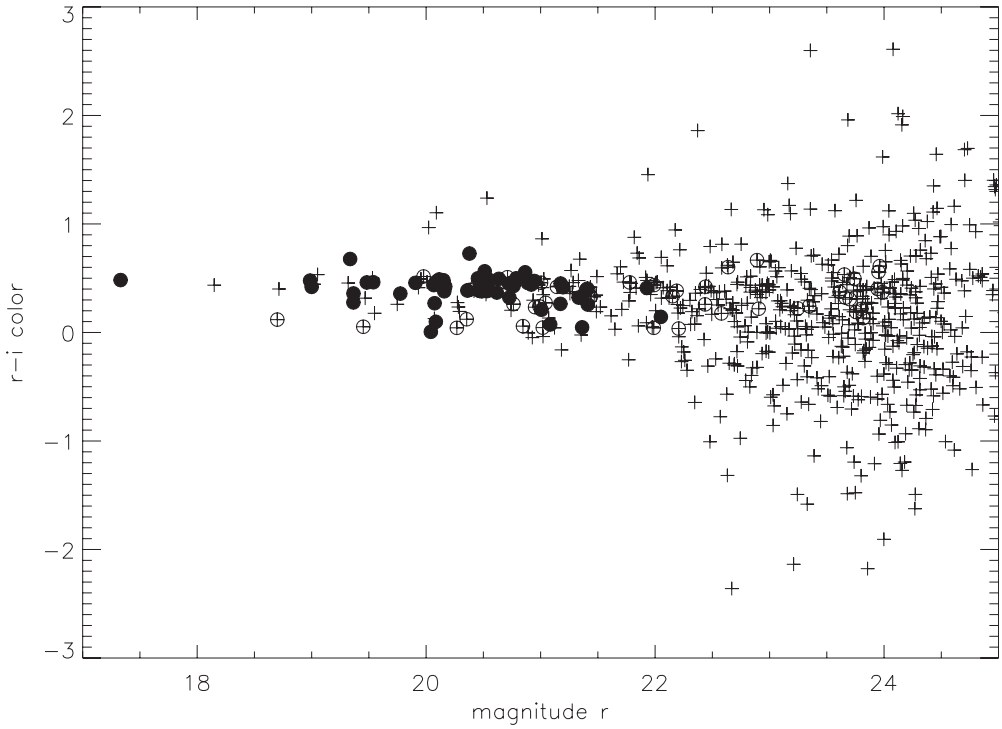


**Figure 2.** Color–magnitude diagram derived from GMOS-South data for galaxies in the AS1063 field. The crosses show all the likely galaxies in this field (CLASS-STAR $< 0.8$). The circles show the cluster galaxy subsample that we derived (i.e., they had colors in the $0. < r' - i' < 0.8$ range and were brighter than $m_{r'}$ of 24.5) and that we could fit on the four masks. Of these, the solid circles show the spectroscopically confirmed cluster members.

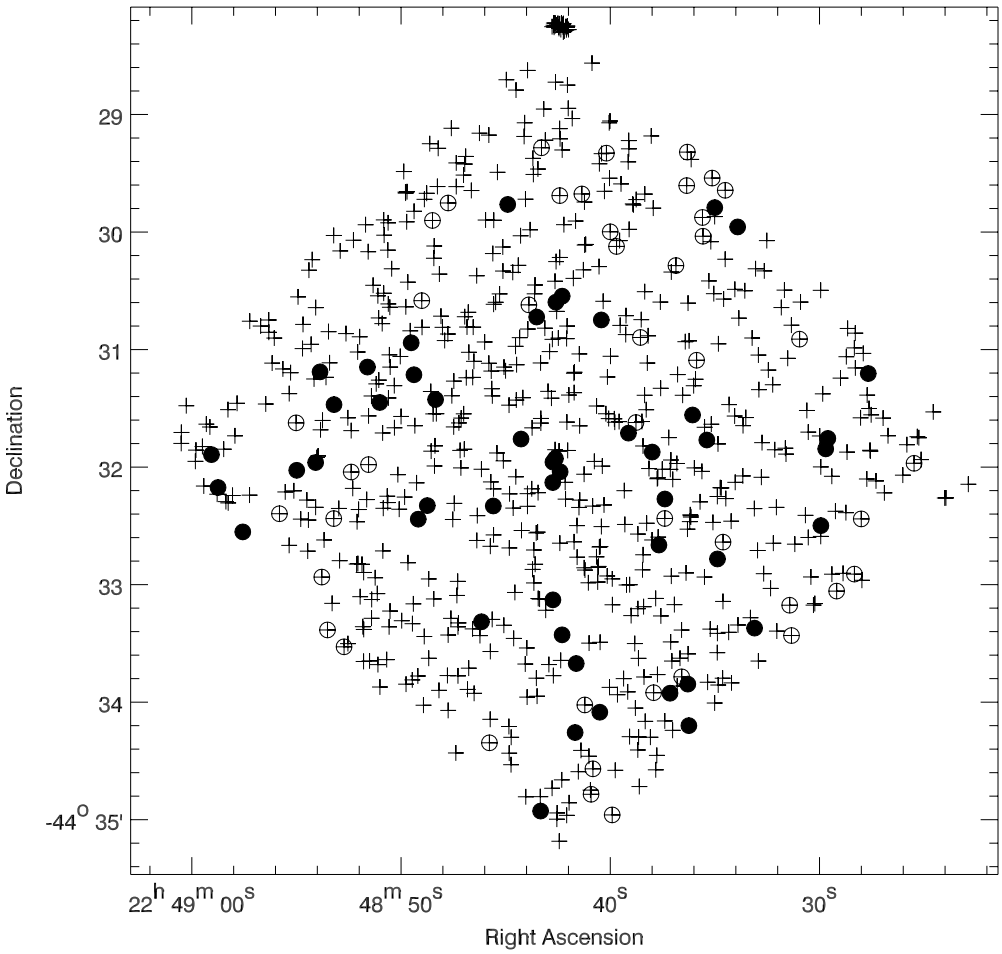


**Figure 3.** Distribution of galaxies in the AS1063 field derived from GMOS-South data. The crosses show all the likely galaxies in this field (CLASS-STAR $< 0.8$). The circles show the cluster galaxy subsample that we derived (i.e., they had colors in the $0. < r' - i' < 0.8$ range and were brighter than $m_{r'}$ of 24.5) and that we could fit on the four masks. Of these, the solid circles show the spectroscopically confirmed cluster members.

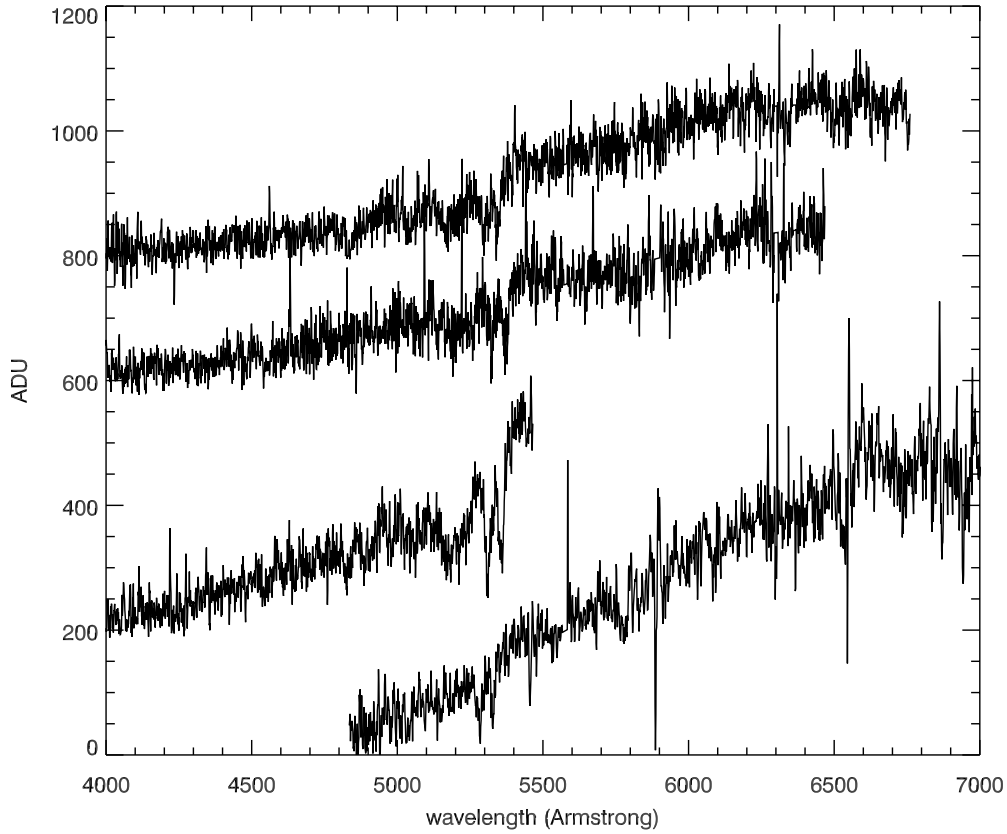


**Figure 4.** Typical spectra extracted from each of the four GMOS masks (only the overlapping spectrum regions are shown). The spectra have been shifted vertically by adding an arbitrary ADU value for clarity. No correction for telluric absorption has been applied to these data.

**Table 1**
GMOS-South Spectroscopic Setup

| Mask | Grating Ruling Density (lines $mm^{-1}$) | Central Wavelength (Å) | Full Range (Å) | Blaze Wavelength (Å) |
|---|---|---|---|---|
| mask1 | 600 | 5300, 5500 | 2760 | 4610 |
| mask2 | 600 | 5300, 5500 | 2760 | 4610 |
| mask3 | 600 | 4600, 4800 | 2760 | 4610 |
| mask4 | 400 | 7800, 8000 | 4160 | 7640 |

of the slits assigned to the arcs were chosen by examining the high-resolution SuSI2 images. Table 1 shows the setups used for the four masks. All the masks were designed with 1 arcsec slits. The slit lengths were ∼2 arcsec longer than the reported maximum length of the object as reported by SExtractor. If the position angle of the galaxy was between 0° and ±30°, then the slit orientation was similar so that we could maximize the amount of galaxy light collected. Masks 1 and 2 were designed to maximize the redshift yield from cluster members, by centering the spectra on the redshifted wavelength (i.e., ∼5300 Å) of the Ca II K and H line break for a $z \simeq 0.35$ galaxy. The other two masks were designed to allow both the detection of emission lines from the three gravitational arcs (see Figure 1) and the measurement of redshifts for candidate cluster members. Since the redshifts of the lensed galaxies were unknown, masks 3 and 4 had a wide spectral coverage (3800 Å to 9000 Å), which is sufficient to detect any obvious emission lines for a galaxy out to $z = 2$.

The spectroscopic observations were carried out in 2003 September in queue mode. The total exposure time was 3600 s per mask, split into two 1800 s exposures to minimize contamination by cosmic rays. The two 1800 s frames were shifted in central wavelength to minimize the effects of bad pixels and the gaps between the three GMOS chips. We used the Gemini IRAF package to reduce the spectroscopy data. First the spectra were bias corrected and flat fielded. Next, we mosaicked the science and arc frames and wavelength calibrated the arc image row by row. We used the calibrated arc image to correct for any distortions and tilt in the slits by shifting the arc rows so that each column in the image corresponds to the same wavelength. We visually verified that these corrections were acceptable before applying them to the science data. We then proceeded to define the galaxy apertures and extract the object and sky spectra from each individual frame. The two 1800 s spectra were co-added by shifting them to a common wavelength frame. We used night sky lines to correct for any offsets introduced by using arcs obtained in the afternoon, i.e., several hours before our observations. This proved to be especially important for masks 3 and 4, possibly due to an improper calibration of the grating between observations on the sky and of the arc lamp. We find that our final spectra were well calibrated with overall errors in the wavelength calibration of <1 Å. Figure 4 shows representative examples of the sky-subtracted spectra for the four masks used in our analysis.

We used the IRAF task FXCOR to compute the recessional velocities for our galaxies. This task allowed us to cross-correlate the observed spectra (after removal of cosmic rays and masking regions containing bright emission lines) with high signal-to-noise templates for different galaxy types obtained from the Sloan Digital Sky Survey database. In addition, we visually examined the spectra, especially the lens spectra, to look for emission lines to confirm the FXCOR results. Table 2 lists the coordinates (J2000) for the 116 objects observed using the four masks, plus their heliocentric recessional velocities and errors, where available. The error on the recessional velocity was computed by adding in quadrature the standard deviation of the template fits plus the error due to the wavelength calibration ($\sim$60 km s$^{-1}$). For galaxies with only emission lines, we computed their errors by adding in quadrature the error due to the wavelength calibration ($\sim$60 km s$^{-1}$) and the error in the position of the night sky lines ($\sim$1.0 Å or $\sim$60 km s$^{-1}$). Some of the galaxies were observed using more than one mask and provided us with an another estimate of the velocity errors. For these galaxies, the standard deviation is $\sim$45 kms$^{-1}$, which lies well within the error determined from the wavelength calibration.

### 2.3. Analysis and Interpretation of the Optical Data

#### 2.3.1. Completeness of the Spectroscopic Sample

After reducing and processing the spectroscopic data, we were able to measure the recessional velocity for 81 of the 116 objects targeted in the slit masks (Table 2). Although our sampling is not complete, we believe that it is representative of the galaxy population in AS1063. For example, of the galaxies targeted for spectroscopy, we have been able to measure the redshift for roughly 50% of those brighter than $r' = 22$ (and roughly 30% at $r' = 24$). We have also compared the radial distribution of the 81 galaxies with measured redshifts to the 329 galaxies selected as candidate cluster members using the color–magnitude relation (see Section 2.2). We computed the ratio of the number of galaxies with redshifts, to the number of candidate members without, for three radial bins, each 1.′0 (270 kpc) wide and centered on the brightest galaxy in the cluster. We obtained values of 0.17, 0.28, and 0.31 for the ratios in the three bins. This distribution shows that we picked relatively more galaxies toward the outskirts of the cluster. This is to be expected for two reasons. First, the cluster core is densely populated making it difficult to design slit masks. Second, two of the masks were designed primarily to obtain spectra for the arcs. The arcs are located within 30″ of the cluster center, making it difficult to assign slits for other objects in the core.

#### 2.3.2. Mean Redshift and Velocity Dispersion

The 81 galaxies with redshifts in Table 2 include cluster members, foreground, and background galaxies and one (of the three) lens candidates. We used an iterative $3\sigma$ clipping criterion (Yahil & Vidal 1977) to identify the cluster members. Most of the outliers were easily rejected after the first iteration. Thus we were left with 51 cluster members (labeled as such in Table 2). Their location and redshift histogram are shown in Figures 5 and 6, respectively. The density of cluster candidates and spectroscopically confirmed members, versus position in the X-ray image, is shown in Figures 7 and 8, respectively. As we are dealing with small number statistics, we used robust biweight estimators for the mean and velocity dispersion in order to characterize the distribution of redshifts (Danese et al. 1980). We used the well known ROSTAT program (Beers et al. 1990) to compute these estimators and their uncertainties. We measured a redshift for the cluster of $z = 0.3461^{+0.0010}_{-0.0011}$ ($1\sigma$ errors) with a velocity dispersion (cosmologically corrected) of $\sigma_{\rm vel} = 1840^{+230}_{-150}$ km s$^{-1}$ ($1\sigma$ errors). We note that this redshift agrees with that quoted in Böhringer et al. (2004) and so the previous confusion over the cluster redshift has been resolved (Section 1).

We note that due to the fact that the GMOS field only samples the inner 2.′7 (or 730 kpc) of the cluster the velocity dispersion could be biased and overestimate the actual value by as much as 4%. This is based on the analysis of the velocity dispersion radial profile present in isothermal King Models (see Binney & Tremaine 2008). We have decided to use a conservative correction factor of $\sim$10% to the velocity dispersion so that the effective velocity dispersion $\sigma_{\rm vel,eff} = 1660^{+230}_{-150}$ km s$^{-1}$.

#### 2.3.3. Cluster Mass

We have computed the mass of the cluster by using the $M_{200}$–$\sigma_{\rm DM}$ scaling relation from Evrard et al. (2008):

$$\sigma_{\rm DM} = \sigma_{\rm DM,15}\left[\frac{h(z)M_{200}}{10^{15}\,M_{\odot}}\right]^{\alpha}, \quad (1)$$

where $M_{200}$ is the mass within a radius where the overdensity is 200 times the critical density of the universe, the exponent $\alpha = 0.3361 \pm 0.0026$, $\sigma_{\rm DM,15}$ is the normalization at mass $10^{15}\,M_{\odot} = 1082.9 \pm 4$ km s$^{-1}$, $\sigma_{\rm DM}$ is the velocity dispersion of the dark matter halo, and $h(z) = H(z)/75$ km s$^{-1}$ Mpc$^{-1}$. In our case, we use the effective velocity dispersion of $\sigma_{\rm vel,eff} = 1660^{+200}_{-135}$ km s$^{-1}$ as a proxy for the dark matter velocity dispersion due to the fact that galaxies are unbiased tracers of the dark matter (see Evrard et al. 2008 for a discussion regarding this issue). We calculated a value of $M_{200} = 3.97^{+1.6}_{-0.9} \times 10^{15}\,M_{\odot}$ and an $r_{200} = 3150^{+300}_{-200}$ kpc, which includes a statistical error and is dominated by the velocity dispersion error.

#### 2.3.4. Dynamical State

In order to determine the dynamical state of the cluster, we examined in more detail the velocity and spatial distribution of the galaxies using one-dimensional (1D), two-dimensional (2D), and three-dimensional (3D) statistical tests. The 1D statistical tests were used to look for non-Gaussianity and/or substructure in the velocity distribution. The 2D tests were used to look for asymmetries and substructure in the spatial distribution of the galaxies. Finally, the 3D tests, which combine the velocity and position information, were used to look for other merger signatures.

There is only marginal evidence for substructure in the velocity distribution of the galaxies. The ROSTAT battery of tests, when run on this velocity distribution (Figure 6), revealed only marginal evidence for non-Gaussianity and a gap in the cumulative distribution of the velocities with respect to a Gaussian distribution. The evidence for kurtosis is also low (probability of normality is $\sim$15%), as measured by the B1 and I tests (Beers et al. 1990).

Next we examined the galaxy density distribution. Figure 7 shows that the confirmed cluster members have a bimodal distribution aligned along the direction of the X-ray elongation. This bimodality is also visible in Figure 8 in the distribution of the 329 galaxies selected as potential cluster members based on their location in the color–magnitude diagram. Figure 9 shows a cut that runs along the two main galaxy clumps from Figure 8. This

**Table 2**
Spectroscopic Targets

| ID | R.A. (2000) | Decl. (2000) | Redshift | Error (km s$^{-1}$) | Notes |
|---|---|---|---|---|---|
| 67 | 22 48 57.247 | −44 32 38.21 | 0.3383 | 109 | Member |
| 70 | 22 48 49.460 | −44 33 55.96 | ... | ... | |
| 72 | 22 48 53.208 | −44 33 28.26 | ... | ... | |
| 75 | 22 48 52.419 | −44 33 36.87 | ... | ... | |
| 79 | 22 48 58.427 | −44 32 15.54 | 0.3477 | 83 | Member |
| 104 | 22 48 42.142 | −44 35 16.17 | 0.3387 | 60 | Member |
| 106 | 22 48 43.032 | −44 35 00.76 | 0.3480 | 89 | Member |
| 118 | 22 48 43.976 | −44 31 50.87 | 0.3471 | 72 | Member, BCG |
| 119 | 22 48 58.747 | −44 31 58.75 | 0.3405 | 77 | Member |
| 130 | 22 48 45.481 | −44 34 25.91 | ... | ... | |
| 133 | 22 48 53.479 | −44 33 01.29 | 0.4570 | 85 | O II emission line |
| 165 | 22 48 55.499 | −44 32 28.95 | 0.4381 | 61 | |
| 194 | 22 48 52.910 | −44 32 31.43 | 0.2977 | 80 | |
| 264 | 22 48 39.614 | −44 35 02.72 | 0.2547 | 67 | |
| 275 | 22 48 40.534 | −44 34 39.20 | 0.0525 | 60 | |
| 276 | 22 48 40.624 | −44 34 52.19 | ... | ... | |
| 279 | 22 48 54.680 | −44 32 06.78 | 0.3458 | 106 | Member |
| 291 | 22 48 51.252 | −44 32 03.90 | 0.0812 | 71 | |
| 297 | 22 48 40.654 | −44 34 50.05 | ... | ... | |
| 309 | 22 48 45.853 | −44 33 24.14 | 0.3354 | 88 | Member |
| 325 | 22 48 53.780 | −44 32 02.82 | 0.3457 | 84 | Member |
| 326 | 22 48 46.982 | −44 33 26.72 | ... | ... | |
| 330 | 22 48 41.384 | −44 34 20.67 | 0.3423 | 114 | Member |
| 379 | 22 48 54.700 | −44 31 42.58 | 0.3671 | 636 | |
| 381 | 22 48 40.925 | −44 34 06.59 | 0.4605 | 150 | |
| 383 | 22 48 52.071 | −44 32 07.68 | 0.2362 | 61 | |
| 388 | 22 48 38.315 | −44 34 48.25 | ... | ... | |
| 389 | 22 48 40.205 | −44 34 10.30 | 0.3375 | 80 | Member |
| 395 | 22 48 51.331 | −44 32 21.76 | 0.2270 | 100 | $H_\alpha$ emission line |
| 403 | 22 48 53.561 | −44 31 16.56 | 0.3475 | 78 | Member |
| 426 | 22 48 48.872 | −44 32 31.75 | 0.3552 | 69 | Member |
| 435 | 22 48 48.443 | −44 32 24.83 | 0.3632 | 92 | Member |
| 457 | 22 48 52.901 | −44 31 33.28 | 0.3407 | 77 | Member |
| 458 | 22 48 41.335 | −44 33 45.45 | 0.3429 | 115 | Member |
| 470 | 22 48 35.957 | −44 34 17.15 | 0.3355 | 71 | Member |
| 497 | 22 48 42.005 | −44 33 30.83 | 0.3459 | 84 | Member |
| 523 | 22 48 42.455 | −44 33 12.95 | 0.3329 | 130 | Member |
| 528 | 22 48 50.723 | −44 31 32.19 | 0.3623 | 77 | Member |
| 559 | 22 48 36.727 | −44 34 19.55 | ... | ... | |
| 575 | 22 48 45.295 | −44 32 25.04 | 0.3477 | 76 | Member |
| 577 | 22 48 36.857 | −44 34 00.61 | 0.3528 | 84 | Member |
| 587 | 22 48 37.637 | −44 34 00.33 | 0.83 | 100 | O II emission line |
| 593 | 22 48 51.303 | −44 31 14.13 | 0.3459 | 72 | Member |
| 601 | 22 48 36.308 | −44 33 52.23 | 0.1976 | 368 | |
| 624 | 22 48 46.935 | −44 31 42.66 | ... | ... | |
| 624 | 22 48 46.935 | −44 31 42.66 | ... | ... | Lens candidate B |
| 634 | 22 48 36.008 | −44 33 55.97 | 0.3464 | 118 | Member |
| 637 | 22 48 49.084 | −44 31 18.06 | 0.3567 | 126 | Member |
| 656 | 22 48 49.214 | −44 31 01.76 | 0.3416 | 84 | Member |
| 667 | 22 48 43.185 | −44 32 38.41 | ... | ... | |
| 702 | 22 48 48.044 | −44 31 30.69 | 0.3523 | 72 | Member |
| 733 | 22 48 46.715 | −44 31 38.02 | ... | ... | Lens candidate C |
| 746 | 22 48 42.456 | −44 32 13.08 | 0.3364 | 71 | Member |
| 779 | 22 48 42.107 | −44 32 07.60 | 0.3362 | 60 | Member |
| 835 | 22 48 42.447 | −44 32 02.66 | 0.3342 | 80 | Member |
| 844 | 22 48 37.389 | −44 32 44.98 | 0.3312 | 82 | Member |
| 850 | 22 48 42.327 | −44 32 00.88 | 0.3461 | 103 | Member |
| 878 | 22 48 41.747 | −44 31 56.72 | 0.6100 | 100 | Lens candidate A, emission line |
| 907 | 22 48 32.820 | −44 33 27.38 | 0.3484 | 226 | Member |
| 934 | 22 48 48.705 | −44 30 40.22 | ... | ... | |
| 966 | 22 48 41.778 | −44 31 42.25 | ... | ... | |
| 984 | 22 48 31.061 | −44 33 31.15 | ... | ... | |
| 993 | 22 48 37.119 | −44 32 31.42 | ... | ... | |
| 996 | 22 48 34.600 | −44 32 52.08 | 0.3479 | 68 | Member |
| 998 | 22 48 37.109 | −44 32 21.49 | 0.3535 | 89 | Member |

**Table 2**
(Continued)

| ID | R.A. (2000) | Decl. (2000) | Redshift | Error (km s$^{-1}$) | Notes |
|---|---|---|---|---|---|
| 1013 | 22 48 36.030 | −44 32 36.87 | ... | ... | |
| 1015 | 22 48 38.849 | −44 31 47.87 | 0.3470 | 83 | Member |
| 1081 | 22 48 24.308 | −44 31 36.99 | ... | ... | |
| 1141 | 22 48 35.324 | −44 29 57.80 | ... | ... | |
| 1163 | 22 48 25.217 | −44 32 03.21 | 0.1122 | 63 | |
| 1178 | 22 48 39.902 | −44 29 24.98 | 0.2409 | 60 | |
| 1199 | 22 48 43.598 | −44 30 42.41 | 0.5341 | 62 | |
| 1255 | 22 48 43.000 | −44 29 22.23 | ... | ... | |
| 1263 | 22 48 28.903 | −44 33 08.45 | ... | ... | |
| 1269 | 22 48 29.335 | −44 31 50.54 | 0.3420 | 99 | Member |
| 1277 | 22 48 40.002 | −44 29 44.44 | ... | ... | |
| 1285 | 22 48 36.593 | −44 30 22.35 | ... | ... | |
| 1289 | 22 48 29.434 | −44 31 55.88 | 0.3497 | 97 | Member |
| 1310 | 22 48 41.081 | −44 29 45.79 | 0.4729 | 67 | |
| 1319 | 22 48 39.721 | −44 30 05.12 | 0.2751 | 176 | |
| 1357 | 22 48 27.735 | −44 32 31.60 | 0.1822 | 220 | |
| 1364 | 22 48 43.228 | −44 30 48.61 | 0.3512 | 142 | Member |
| 1367 | 22 48 42.130 | −44 29 46.63 | ... | ... | |
| 1381 | 22 48 41.380 | −44 29 59.64 | 0.4535 | 60 | |
| 1386 | 22 48 39.421 | −44 30 12.60 | 0.1800 | 100 | $H_\alpha$ emission line |
| 1410 | 22 48 35.602 | −44 31 10.66 | 0.6110 | 100 | O II emission line |
| 1453 | 22 48 29.663 | −44 32 35.04 | 0.3382 | 78 | Member |
| 1472 | 22 48 44.609 | −44 29 51.15 | 0.3553 | 85 | Member |
| 1482 | 22 48 38.281 | −44 30 59.05 | ... | ... | |
| 1500 | 22 48 28.054 | −44 32 59.77 | ... | ... | |
| 1501 | 22 48 42.309 | −44 30 41.03 | 0.3553 | 72 | Member |
| 1503 | 22 48 40.140 | −44 30 50.11 | 0.3509 | 65 | Member |
| 1532 | 22 48 35.111 | −44 31 51.37 | 0.3525 | 76 | Member |
| 1546 | 22 48 42.019 | −44 30 37.97 | 0.3436 | 94 | Member |
| 1592 | 22 48 47.457 | −44 29 50.40 | ... | ... | |
| 1610 | 22 48 38.490 | −44 31 42.46 | 0.4569 | 61 | |
| 1613 | 22 48 35.341 | −44 32 07.40 | ... | ... | |
| 1645 | 22 48 48.206 | −44 29 59.31 | ... | ... | |
| 1647 | 22 48 33.645 | −44 30 02.62 | 0.3541 | 81 | Member |
| 1661 | 22 48 37.710 | −44 31 57.53 | 0.3455 | 87 | Member |
| 1662 | 22 48 35.791 | −44 31 38.60 | 0.3356 | 81 | Member |
| 1677 | 22 48 32.061 | −44 33 07.12 | ... | ... | |
| 1684 | 22 48 30.132 | −44 33 01.25 | 0.2472 | 63 | |
| 1689 | 22 48 31.141 | −44 33 15.68 | ... | ... | |
| 1703 | 22 48 34.330 | −44 32 43.49 | 0.4518 | 100 | O II emission line |
| 1790 | 22 48 36.044 | −44 29 24.45 | 0.0562 | 60 | |
| 1796 | 22 48 34.865 | −44 29 37.69 | 0.4559 | 98 | |
| 1800 | 22 48 34.245 | −44 29 43.93 | ... | ... | |
| 1842 | 22 48 27.407 | −44 31 17.41 | 0.3482 | 85 | Member, emission and absorption |
| 1848 | 22 48 34.734 | −44 29 52.76 | 0.3598 | 82 | Member |
| 1867 | 22 48 36.074 | −44 29 41.53 | 0.1502 | 79 | |
| 1884 | 22 48 35.304 | −44 30 07.37 | 0.5850 | 300 | O II emission line |
| 1900 | 22 48 27.456 | −44 31 28.44 | ... | ... | |
| 1908 | 22 48 24.887 | −44 32 01.29 | ... | ... | |
| 1928 | 22 48 30.685 | −44 30 59.89 | 0.4434 | 300 | O II emission line |
| 2000 | 22 48 43.80 | −44 31 49.83 | 0.3482 | 65 | Member, close to central galaxy |

cut was made at an angle of 51°.3 measured counterclockwise from the north. Later on we will show that this value runs almost parallel to the elongation of the X-ray isophotes, which changes from 70° to 60°. The projected distance between the two main galaxy density clumps is $\sim 120 \pm 12$ arcsec or $490 \pm 55$ kpc in Figure 8. The distance is slightly larger (by 10 arcsec) in Figure 7. If we fit each galaxy clump with a Gaussian function, we estimate that the ratio of the number of galaxies in them is ∼1.5. The third clump in Figure 9 and located at 360′ is an artifact produced by the smoothing algorithm applied to the density map and provides a measure of the noise in the map. We assess the significance of the substructure by running a series of four tests. The angular separation (West et al. 1988) test; the so-called $\beta$ test (West et al. 1988); the Fourier elongation test (Pinkney et al. 1996); and the Lee statistic (Lee 1979; Fitchett & Webster 1987). The first three did not detect any significant 2D substructure. Only the Lee statistic rejected the null (i.e., no substructure) hypothesis at the 90% level. This method uses the maximum likelihood statistic to determine the significance of splitting 2D data into subgroups.

We also looked for substructure using 3D tests that consider both the spatial and kinematical positions of the galaxies. Please

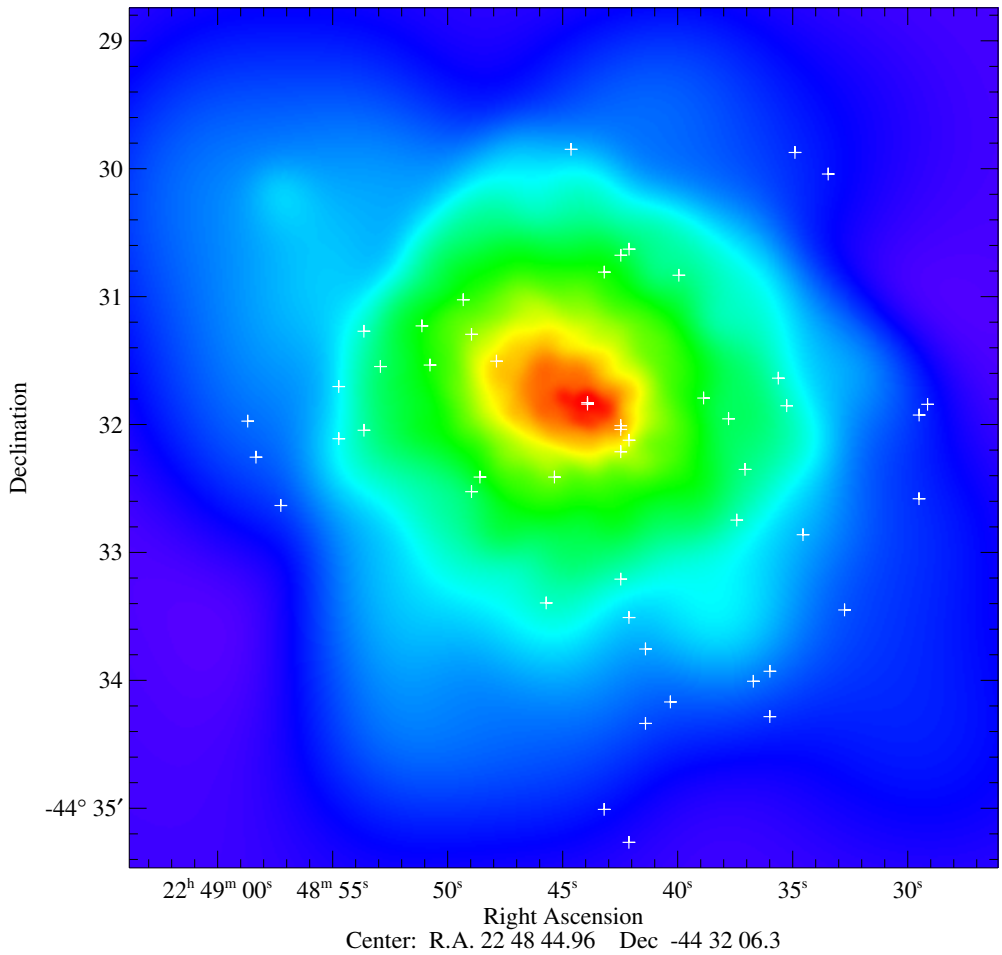


**Figure 5.** Smoothed *Chandra* image of the cluster in the 0.2–10 keV energy range. The white crosses represent the positions of the 51 spectroscopically confirmed cluster members. Note that the X-ray emission is elongated in the NW–SE direction.

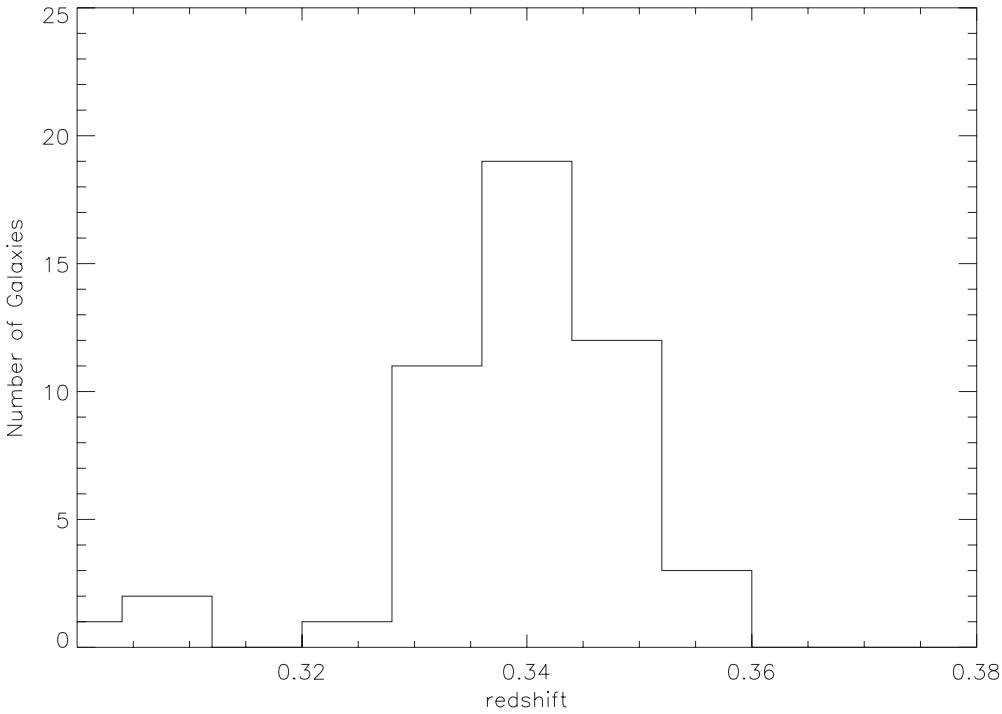


**Figure 6.** Velocity histogram of the galaxies in AS1063. The bin size is 2400 km $s^{-1}$.

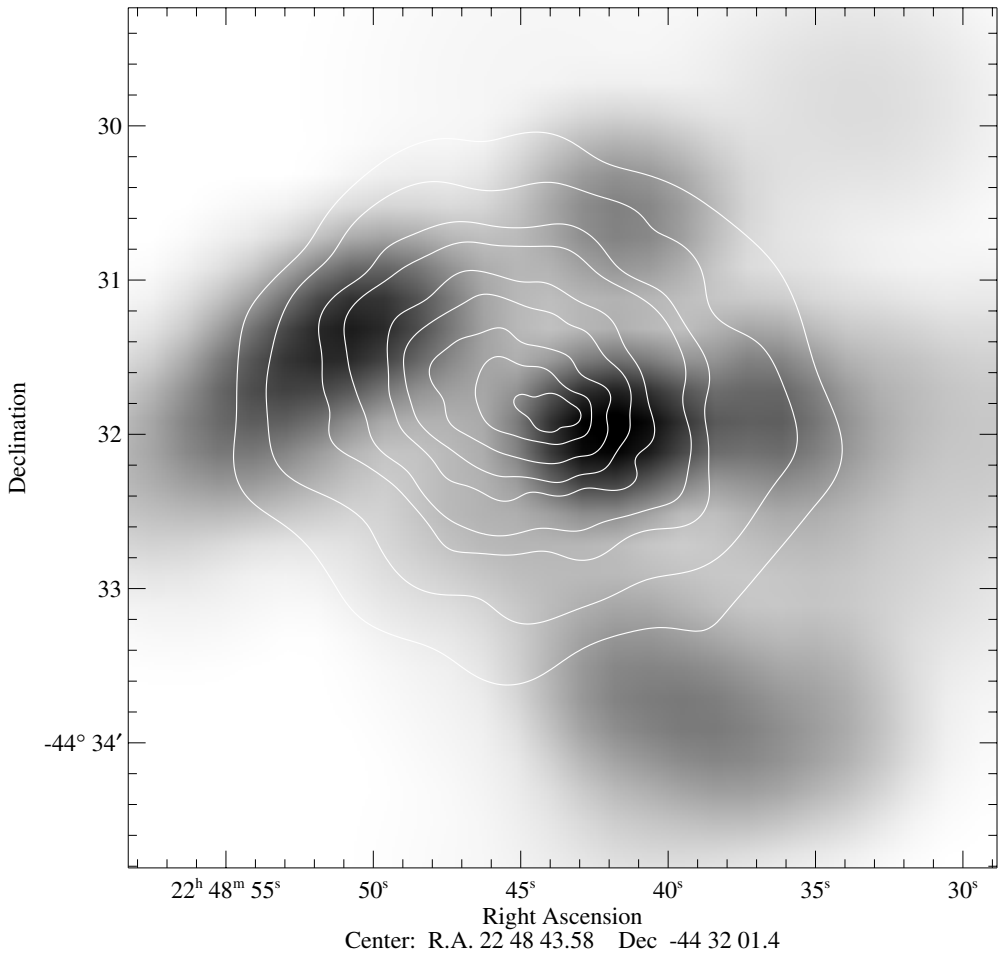


**Figure 7.** Overlay of the smoothed 0.2–10 keV X-ray emission (white contours) over a grayscale image of the galaxy density. Here we show the density of the 51 spectroscopically confirmed cluster members. Note that the X-ray peak is slightly offset from the peak in the galaxy density and that the X-ray emission is elongated along the direction connecting the two densest galaxy regions.

note that our spatial sampling of the galaxies is not uniform and this could affect the sensitivity of these tests. We ran three different tests on the data: the Lee 3D (Pinkney et al. 1996); the Dressler–Shectman (Dressler & Shectman 1988); and the $\alpha$ (West & Bothun 1990) tests. The Lee 3D test found significant evidence for substructure, rejecting the null hypothesis at the 99% level. This test is similar to the Lee 2D test and looks for evidence for bimodality in the distribution of the galaxies by weighting the positions with the galaxy velocities. The Dressler–Shectman test calculates a statistic based on comparing the local mean and dispersion velocity for a given galaxy (computed from the nine nearest neighbors) with the global values. Figure 10 shows a representation of this test. Note that there are larger circles on this figure located around the positions of the two peaks in the galaxy density. The significance of this test is found by using the Monte Carlo technique in which the statistic is re-calculated by reshuffling the velocity data among the cluster members. The test finds that only $\sim$10% of the trials show a larger statistic (i.e., stronger evidence for substructure) than the real distribution. Finally, the $\alpha$ test does not find evidence for substructure. This test determines the shift in the galaxy centroid position by the presence of correlations between the local velocity and spatial galaxy distribution from subgroups assembled from the 10th nearest neighbors.

In summary, the strongest optical evidence for a merging event comes from the galaxy density distribution (Figures 7–9), which shows a bimodality consistent with that seen in the X-ray image. This substructure is confirmed by the results of the Lee 2D and Lee 3D statistics and marginally by the Dressler–Shectman test. It is worth mentioning that there is no single test that can determine the dynamical state of every cluster (Pinkney et al. 1996). Therefore, it is not surprising that some tests yield inconclusive results. After all, the sensitivity of a given test to detect substructure (or other perturbations such as asymmetry) depends on both the quality and completeness of the data available and on the properties of the merging system, such as mass ratio, merger epoch, and viewing angle (e.g., Pinkney et al. 1996; White et al. 2010). Thus, a more insightful approach would be to compare the observables with numerical simulations. This approach has already been applied with success to other clusters (e.g., Springel & Farrar 2007). We describe an initial attempt at this type analysis in the next section.

#### 2.3.5. Comparison with N-body Numerical Simulations

Significant bimodality in the spatial distribution and/or velocity distribution only occurs during certain merger epochs, mass ratios, and viewing angles. For instance, if a merger happens in the plane of the sky then the spatial distribution of gas and galaxies would be bimodal anytime before core crossing and at some epochs after core crossing. If the merger happens along the line of sight then the velocity distribution of the two clusters is

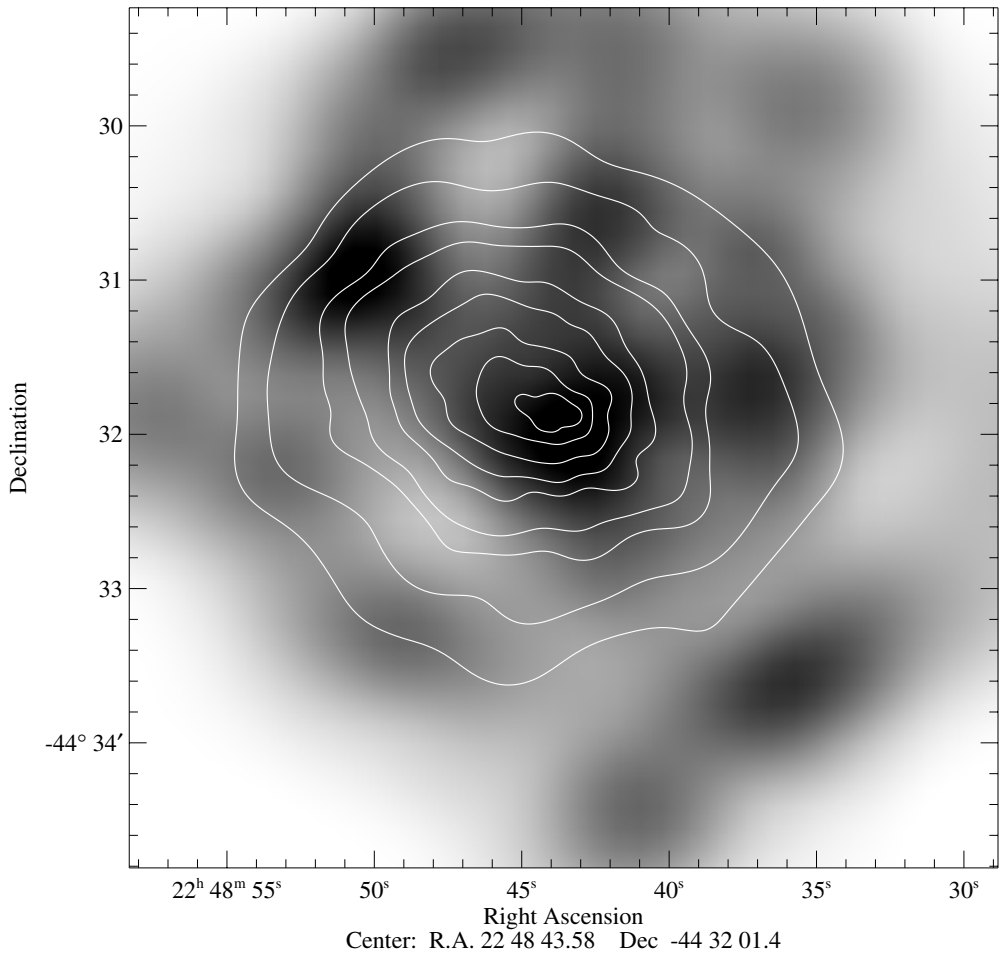


**Figure 8.** Overlay of the smoothed 0.2–10 keV X-ray emission (white contours) over a grayscale image of the galaxy density. Here we show the density of 329 candidate cluster members, as selected using the color–magnitude diagram.

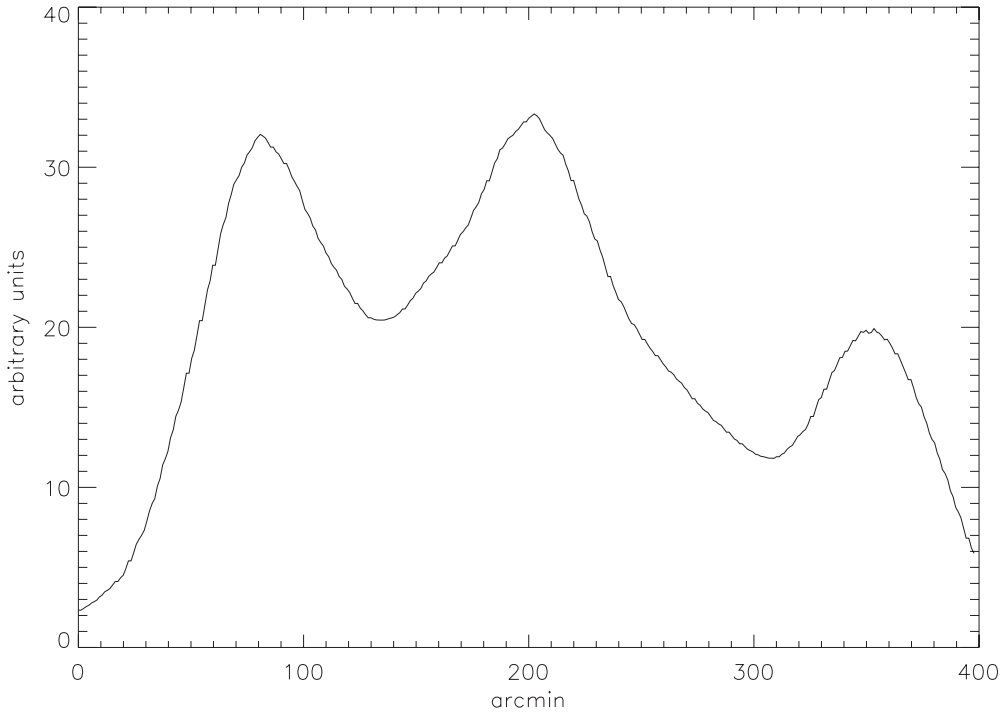


**Figure 9.** Cut that runs along the two main galaxy clumps from Figure 8. This cut was made at an angle of 51.°3 measured counterclockwise from the north.

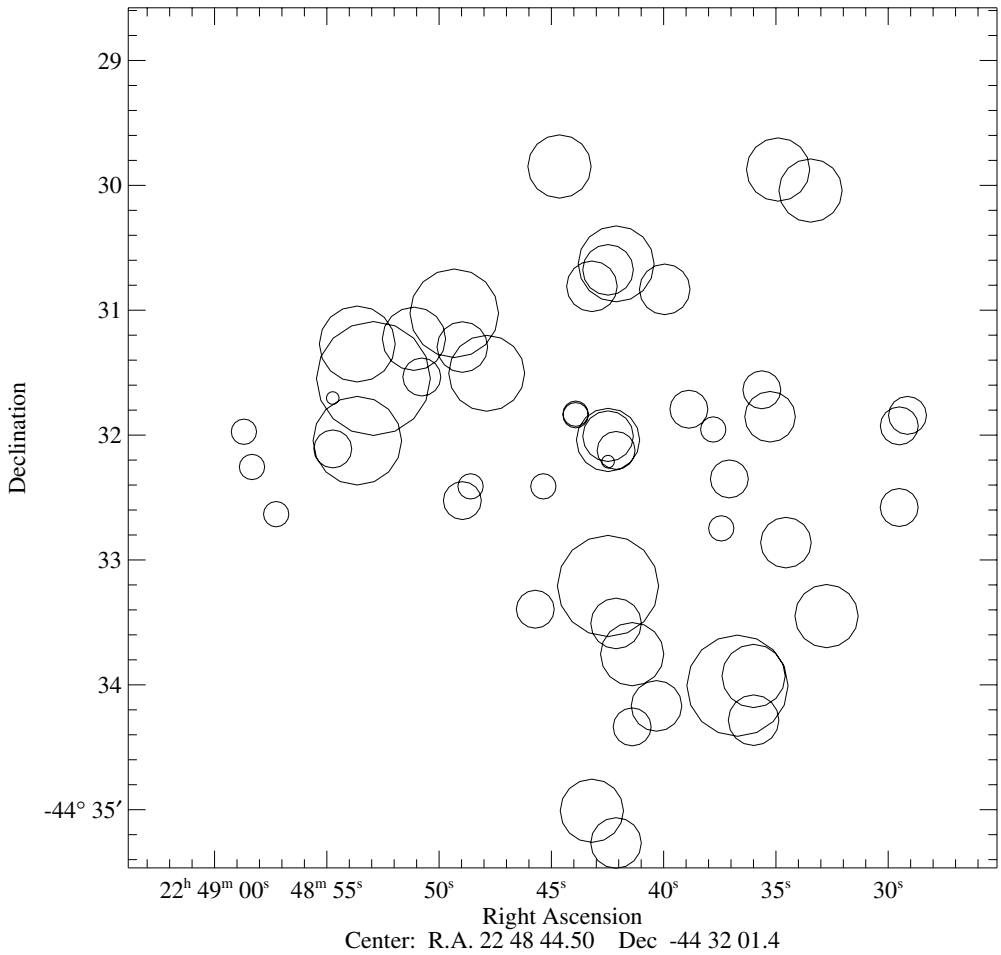


**Figure 10.** Representation of the Dressler–Shectman substructure test. Each circle represents a cluster member and the radius of the circle is proportional to the difference between a given galaxy velocity and the local velocity dispersion (computed from the nine nearest neighbors). Note that there are larger circles located around the positions of the two peaks in the galaxy density. The actual test determines the significance of any substructure by performing a Monte Carlo simulation. In this case, the structure shown is marginally significant at the 90% level.

significantly bimodal right before core crossing (Pinkney et al. 1996). In view of this, we will compare our galaxy data with numerical simulations of cluster mergers and ask the following question. Can we identify a cluster merger type and a merger epoch that will produce a velocity distribution that has a significant probability of being the parent population of the observed velocity distribution?

The *N*-body numerical simulations of 50,000 particles and the method used for comparing the observed and *N*-body velocity distributions are described in detail in Gómez et al. (2000). We will briefly list here the main properties of the numerical simulations. The interaction between the clusters simulates a head-on collision (impact parameter equal to zero) and is idealized as starting from infinity with zero initial velocity. For practical purposes (i.e., to reduce the computational run time), the simulations are started with the two clusters separated by 6 Mpc with a relative velocity of $\sim$1000 km s$^{-1}$. *N*-body particles alone are not perfect tracers of the galaxies but they can be used to derive the spatial and kinematical trends suitable for our work. Our study focused on particles located within 750 kpc from the center of mass which would always be located close to the main cluster due to the mass ratio explored. Furthermore, we used the same radial dependence reported in 2.3.1. Thus, we divide the *N*-body particles in three radial bins: $r < 250$ kpc, 250 kpc $\leqslant r <$ 500 kpc, and 500 kpc $\leqslant r <$ 750 kpc such that the ratios were in agreement with the observations (Section 2.3.1). We concentrated our comparison with mergers with mass ratio 1:4 and 1:16 because they produce clusters with a similar level of substructure as the one seen in AS1063 (e.g., Roettiger et al. 1997; Gómez et al. 2002; Poole et al. 2006). This effort does not try to identify the exact merger responsible for AS1063; our goal is to show that a merger can produce a velocity and spatial distribution of galaxies that are consistent with the observations.

The *N*-body simulations were performed with normalized units. Therefore, in order to compare them with the observations we applied a length and mass scaling. In this way, we probe a parameter space given by main cluster mass from (0.3–3.0) $\times$ $10^{15}$ $M_{\odot}$ with $\sim$4 $\times$ $10^{13}$ $M_{\odot}$ steps; epoch from 6 Gyr before core crossing to 4 Gyr after core crossing with a typical time step of $\sim$0.2 Gyr; and different viewing angles from a merger in the plane of the sky (90°) to a merger along the line of sight (0°) in 5°steps. We found that mergers of the following type yield a Kolmogorov–Smirnov (K-S) probability greater than 0.9 (i.e., we reject all other models at the 90% confidence level, see Figure 11): a mass ratio of 1:4; a main cluster mass of (1.15–1.5) $\times$ $10^{15}$ $M_{\odot}$; a viewing angle of 80°–90°; and a merger epoch of 0.1–3.5 Gyr *after* core crossing. This means that only these models produce velocity distributions that have a 90% probability of having been drawn from the same parent velocity distribution as the observed one. We can further constrain the

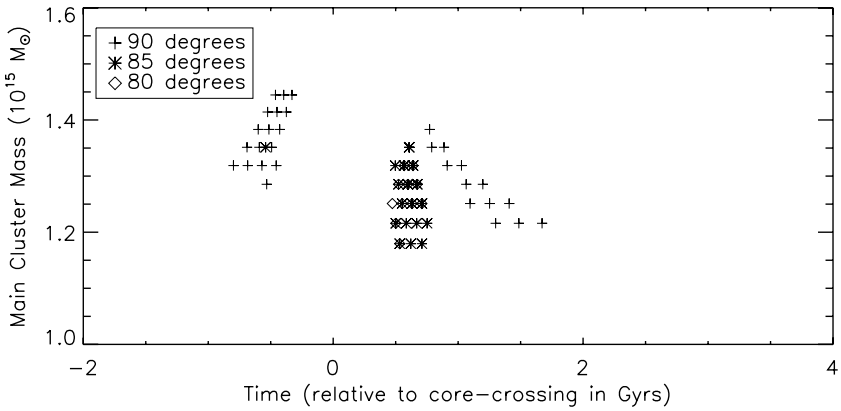


**Figure 11.** Results of comparing the observed velocity distribution with the velocity distribution of *N*-body simulations of cluster mergers. Only the 1:4 mass ratio mergers that produce velocity distributions with a 90% probability of having the same parent population as the observed one (K-S probability greater than 0.9) are plotted. The legend shows the likely viewing angles.

number of possible models by including the distance between the two main galaxy overdensities as an additional parameter. In this way we find that mergers close to the epoch of core crossing (1 Gyr after) and with angles between 80° and 85° yield a spatial distribution consistent with the observations.

As we have mentioned before, we limited our analysis to head-on mergers. These mergers will produce the strongest disruptions on the systems. A rotation term will be added to the merging clusters if the merger is not head-on. We plan to explore these other mergers in the future by comparing the observations with more realistic simulations of cluster evolution.

#### 2.3.6. Central Galaxy

The brightest cluster galaxy (BCG) is located at (J2000) 224844.0, −443150.7. This is galaxy 118 in Table 2. Its recessional velocity is $310^{+310}_{-340}$ km s$^{-1}$ with respect to the cluster mean velocity, which is not a significant peculiar velocity. Interestingly, the optical image reveals three other galaxies located (in projection) closer than 3″ from the BCG. We have measured the recessional velocity of one of these neighbors (galaxy 2000 in Table 2) and found its relative velocity to be $\simeq$650 ± 100 kms$^{-1}$ with respect to the BCG. It is not clear from the available data if these galaxies are physically associated with the BCG.

#### 2.3.7. Gravitational Lenses

The GMOS and SuSI2 images show the presence of several arcs in this cluster (Figure 1). We targeted three of these gravitational arc candidates during the spectroscopic follow-up: lens A, lens B, and lens C. Since we were uncertain as to the redshift for these arcs, we designed the observing setup by using a large wavelength coverage: masks 3 and 4 covered $\simeq$3300 Å < λ < 9700 Å (Table 1). This wavelength range is sufficient to detect any obvious emission lines from a galaxy out to $z \sim 2$.

Of these spectra, only lens A yielded a spectrum of sufficient signal to noise to provide a galaxy redshift. Figure 12 shows the spectral region around the Hβ redshifted emission line for this object. The other arcs do not show emission lines and the exposure time was not long enough to detect their continuum and absorption lines.

It is not possible to model accurately the gravitational potential of the cluster with only one lens redshift. However, we can construct a simple model in order to estimate the mass located inside the region defined by arc system A (we will assume that A and counter-arc A belong to the same source, see Figure 1). We used the parametric method implemented in the LENSTOOL[12] ray-tracing code (Jullo et al. 2007) to model the lens using a dual Pseudo Isothermal Elliptical Mass Distribution (see Elíasdóttir et al. 2007). The dPIEMD can be characterized by seven parameters: the center position $(X, Y)$, the ellipticity $\epsilon$, the position angle $\theta$ (measured counterclockwise from the north), and the parameters of the density profile, velocity dispersion $\sigma_0$, core radius $r_{\rm core}$, and cut radius $r_{\rm cut}$. The coordinates in the position are measured relative to the BCG (see Table 2).

To increase the number of constraints, we decompose arc A in three subcomponents and we associate them with their three respective counter-images in the counter-arc A. This is justified by the fact that the arc is large (over 5″) and that we can derive a recessional velocity for different sections of the lens (see Figure 12). This gives six constraints for our model. Since we have seven parameters in our dPIEMD profile, we fixed $r_{\rm core}$ = 30 kpc and $r_{\rm cut}$ = 1000 kpc (these limits are motivated by the models in 10 X-ray luminous galaxy clusters in the work of Smith et al. 2005) and we let the remaining parameters free with broad uniform priors. Considering an uncertainty in the position of any image equal to at most 0.″2 (pixel size of the images), we found after the optimization in the image plane, a $\chi^2 = 1.8$ for 1 degree of freedom. As we note in Figure 13, the positions of the two magnified subcomponents are reproduced very well by our model, with a mean scatter less than 0.″1. The fit also predicts a third demagnified image; however, this would not be seen as it is located close to the BCG and our observations were not deep enough.

Given the best-fit parameters for the clumps ($X = -12 \pm 2$, $Y = -3 \pm 1$, $\epsilon = 0.57 \pm 0.07$, $\theta = 63 \pm 7$, $r_{\rm core} = 30$ kpc, $\sigma_s = 1389 \pm 17$ km s$^{-1}$, $r_{\rm cut} = 1000$ kpc), we calculated that the total mass inside the region limited by the arc system is

$$M(r < 25'' \quad \text{or} \quad \sim 110\,\text{kpc}) = (1.66 \pm 0.08) \times 10^{14}\, M_\odot. \quad (2)$$

We have also calculated the total mass assuming a spherical mass distribution model. We obtained a mass of $M(r < 25'') = (1.8 \pm 0.2) \times 10^{14}\, M_\odot$, which is in agreement with the estimate derived using the dPIEMD model. We would like to stress that our model is oversimplified, since we are modeling a very complex cluster with a single mass profile. However given the very limited number of observational constraints (one single arc

[12] This software is publicly available at http://www.oamp.fr/cosmology/lenstool/.

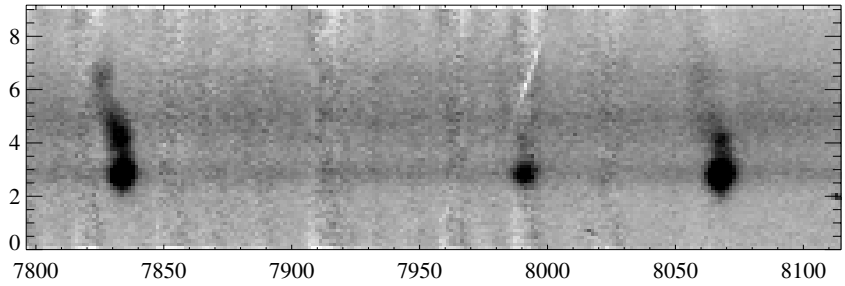


**Figure 12.** Grayscale image of the optical spectrum for lens A. It shows the spectral region around the redshifted H$\beta$ and O[III] emission lines. There is clear kinematical structure in this galaxy as shown by the bending of the BCG spectral lines. The horizontal axis shows the observed wavelength in Å and the vertical axis has the units of arcseconds.

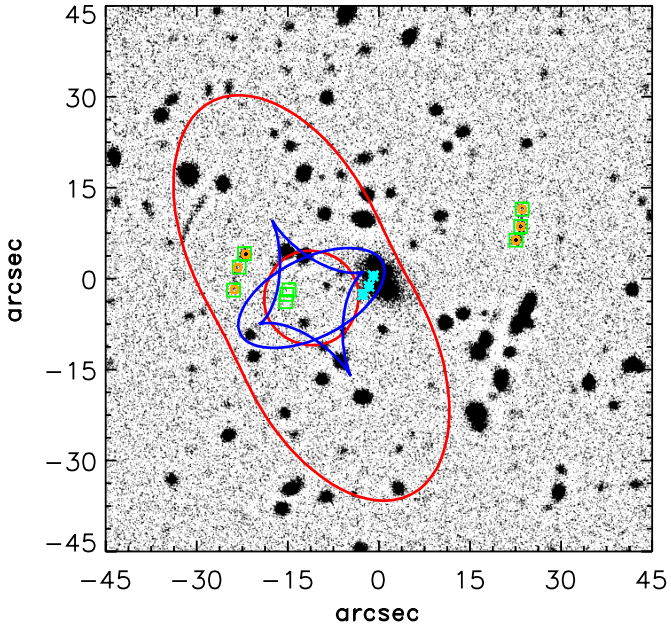


**Figure 13.** *I*-band image of AS1063 with local median average subtracted. North is up and east is left. The external critical line (red line) and the associated caustic line (blue line) for a source at $z = 0.61$ are depicted. Orange circles are the measured image positions and green squares represent the predicted image positions. There is a third set of images but they form close to the center and are demagnified, and therefore, difficult to detect. We also show with small asterisks (cyan) the positions in the source plane associated with these three points.

with redshift) it is not possible to do a more detailed analysis. Even so, we would like to point out that this model shows an elongated mass distribution that is aligned (within the errors) with the direction of the elongation found in the X-ray emitting gas and in the direction of the main clumps of galaxies. This alignment is consistent with a recent merger model for the cluster.

## 3. X-RAY OBSERVATIONS

The *Chandra* satellite observed AS1063 during observing cycle 5 (sequence number 800412) on 2004 May 17. The observations were performed with the four ACIS-I chips and the ACIS-S S2 chip active, for a total on-source time of 27,070 s. The S2 chip was later used to monitor the quiescence of the background. As suggested for observation of faint extended sources, the data were telemetered with the "VFAINT" data mode.

### *3.1. Data Reduction*

We reduced the X-ray data in the usual way using the CIAO software (version 3.3) and the CALDB calibration library (version 3.2.2). First, we created a new level 2 event file from the level 1 event file by applying the latest algorithms and gain maps developed by the Chandra Science Center. For this, we identified and corrected for cosmic ray afterglows and ACIS hot pixels using the task "acis-run-hotpix." This task also creates a new bad pixel file. Next, we used the CIAO task "acis-process-events" to correct the events for time-dependent gain variations and charge transfer inefficiencies. Likewise, the task also applied the gain maps to the data and removed the random pixelation of the pixels introduced by the *Chandra* pipeline. After these corrections were applied, we created the new level 2 event file by only choosing the events that had ASCA grades 0, 2, 3, 4, and 6 and that did not include high background regions. The total exposure time after these cuts were made was 26,604 s.

Figure 5 shows the image of the cluster in the 0.2–10 keV energy range. In order to generate this image, we first identified and removed point sources by using the "wavdetect" task. Then, we adaptively smoothed the image with the "csmooth" task.

### *3.2. Imaging Analysis*

We performed an isophotal analysis of the distribution of the X-ray emission (e.g., Mohr et al. 1993; Mohr et al. 1995) by using the IRAF task ELLIPSE (Jedrzejewski 1987). This task uses an iterative least-squares statistic to model the radially decreasing surface brightness with elliptical isophotes. We let the centroid position, position angle, and ellipticity vary in order to obtain the best fit. Figure 14 shows the results of these fits by displaying how the centroid, position angle, and ellipticity change as a function of radius. This figure shows that there is significant centroid movement, ellipticity variation, and isophotal twisting. Initially, the isophotes are very elliptical and centered on the BCG. But as the fits move to the outer regions, there is a shift in their centroids. For instance, at 1 arcmin from the initial center, the centroids have shifted by as much as 10 arcsec. Beyond 1 arcmin it is also apparent that the isophotes become rounder. It is also interesting to note that there is a rotation in the position angle of the isophotes. They started off with a position angle of 70° and rotate by as much as 10° at a radius of 30 arcsec from the center. At this point, the isophotes become rounder and the ellipticity converges to zero and the position angle becomes meaningless.

A similar analysis was performed by Maughan et al. (2008). They quantified the centroid shifts by following the method of Poole et al. (2006) based on calculating the standard deviation of the centroid shifts calculated at different fractions of $R_{500}$. They reported an overall $\langle w \rangle = 0.74 \pm 0.06$ in units of $10^{-2} R_{500}$. However, they used an incorrect value for the cluster redshift of 0.252. We have converted their $\langle w \rangle$ to arcsec and obtain a value of $\sim 3'' \pm 0\farcs3$. We have calculated the standard deviation

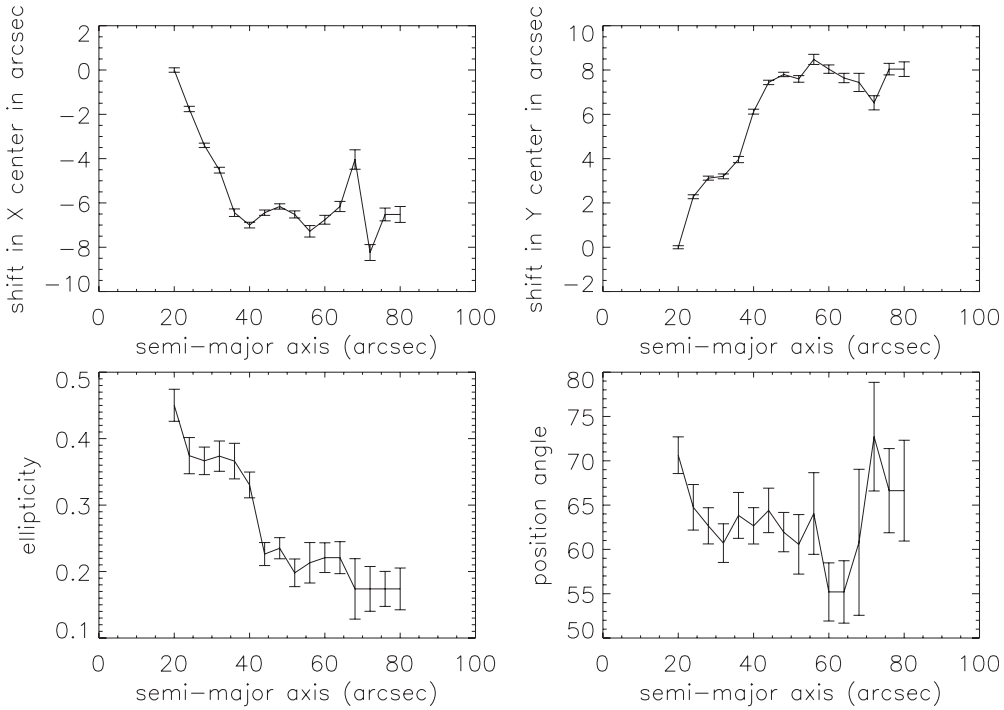


**Figure 14.** Results of elliptical fits to the X-ray emission from the cluster. The top two panels show the shift in the centroid. The bottom left panel shows the ellipticity at each annulus. The bottom right panel shows the position angle in each annulus and its errors (measured as positive counterclockwise from the north). Note that the elongation of the distribution of the X-ray emitting gas is misaligned with respect to the elongation derived with the strong lens model by more than 30°.

**Table 3**
Results of the Single MEKAL Temperature Fits

| Region | Inner and Outer Radius (kpc) | Ellipticity | Temperature[a] (keV) | Error[a] (keV) | Metallicity[a] | Error[a,c] | Temperature[b] (keV) | Error[b] (keV) | Metallicity[b] | Error[b,c] |
|---|---|---|---|---|---|---|---|---|---|---|
| 1[d] | 0 38 | 0 | 13.2 | 3.4 | 0.98 | 0.4 | 11.6 | 1.9 | 0.94 | 0.4 |
| 2[d] | 38 76 | 0 | 13.3 | 1.7 | 0.49 | 0.2 | 12.1 | 1.3 | 0.45 | 0.2 |
| 3 | 76 135 | 0.23 | 15.6 | 2.2 | 0.21 | 0.17 | 14.2 | 1.7 | 0.21 | 0.16 |
| 4 | 135 216 | 0.23 | 11.4 | 1.1 | 0.41 | 0.13 | 10.5 | 0.9 | 0.39 | 0.11 |
| 5 | 216 294 | 0.23 | 16.6 | 2.4 | 0.3 | ... | 14.7 | 1.5 | 0.3 | ... |
| 6 | 294 373 | 0.23 | 14.4 | 1.9 | 0.3 | ... | 12.9 | 2.9 | 0.3 | ... |
| 7 | 373 452 | 0.23 | 12.8 | 3.1 | 0.3 | ... | 11.5 | 1.8 | 0.3 | ... |
| 8 | 452 639 | 0.23 | 16.7 | 9.2 | 0.3 | ... | 14.9 | 2.3 | 0.3 | ... |
| 9 | 639 796 | 0.23 | 15.5 | 4.0 | 0.3 | ... | 13.9 | 6.5 | 0.3 | ... |

**Notes.**
[a] Spectral fits with a fixed $N_{\rm H} = (2.12 \pm 0.9) \times 10^{20}$ cm$^{-2}$.
[b] Spectral fits with a higher fixed $N_{\rm H} = (3.8 \pm 1.4) \times 10^{20}$ cm$^{-2}$.
[c] The metallicity was fixed at 0.3 solar from region 5 outward.
[d] This is a circular region.

of our measurements and derived a value of $3\farcs2 \pm 0\farcs2$, which is in agreement with their value.

### 3.3. Spectroscopic Analysis

We analyzed the spatial distribution of the gas temperature by dividing the cluster into several regions as shown in Table 3. We divided the cluster core into two concentric regions (regions 1 and 2) centered on (J2000) 22 48 43.9, −44 31 49.26 (see Table 5). We used concentric elliptical annuli for the rest of the cluster (see regions 3, 4, 5, 6, 7, 8, and 9 in Table 3), which had a fixed ellipticity, position angle, and centroid as defined by the main component of the double beta-model fit (see Section 3.3.1 and Table 5, Column 2, component 1).

Our spectral fits were performed following the method described by Vikhlinin et al. (2005). We extracted at least 1000 counts from each region in the 0.6–10 keV energy band and rebinned these counts so that we had more than 50 counts in each channel. We excluded two obvious point sources from the cleaned event file located in regions 7 and 8. The spectral fits were performed to a MEKAL model with a single temperature. We left the metal abundance as a free parameter except for the regions at which we obtained an uncertainty >0.2 solar (from region 5 to the edge).

The cluster extended emission fills completely chip 3 and spills to the other three ACIS-I chips. Therefore, we decided to model the background contribution present in the observation by extracting background spectra from the "blank-sky" background files available in the CHANDRA calibration database. These background files were processed in the same way as the cluster data and the events were re-projected onto the sky so that we can extract their spectra by using the same regions used in the

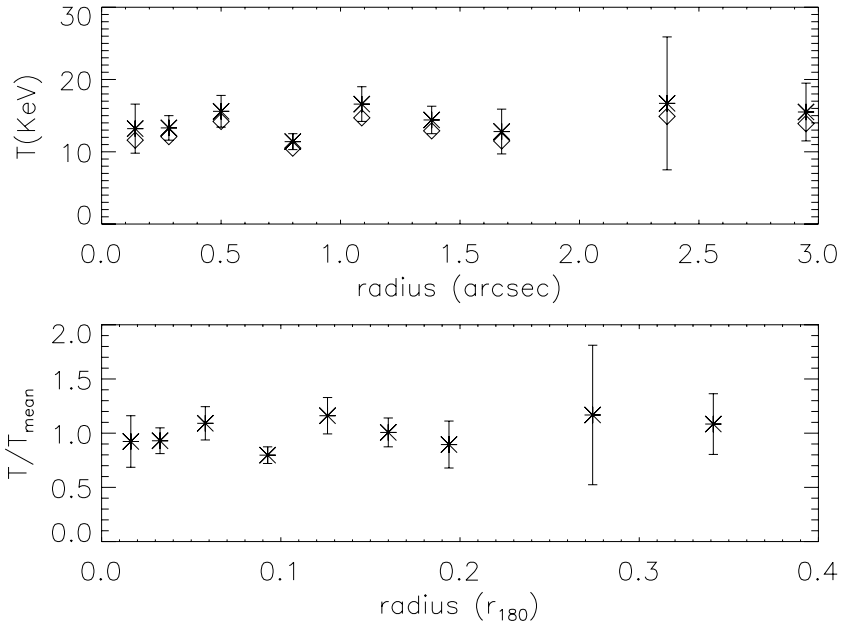


**Figure 15.** Top: the projected X-ray temperature of the cluster gas as a function of radial distance from the X-ray peak ($1' \simeq 270$ kpc). In this case, we show the results assuming $N_{\rm H} = 2.12 \pm 1.1$ and $N_{\rm H} = (3.8 \pm 1.4) \times 10^{20}$ cm$^{-2}$. The error bars correspond to the lower value. Bottom: the normalized temperature profile ($T/T_{\rm mean}$) for the $N_{\rm H}$ value of $(3.8 \pm 1.4) \times 10^{20}$ cm$^{-2}$ fits plotted as a function of the $r_{180}$ radius as shown in Vikhlinin et al. (2005). We used $T_{\rm mean} = 12.5$ keV.

cluster analysis. These background files have a 2% uncertainty due to the inherent limitations in modeling the internal detector background (Vikhlinin et al. 2005). We have compared these background spectra with the spectra extracted from regions in the other chips that have negligible cluster emission. We find minimal residuals with small rms (5%), which are due to the different soft diffuse X-ray present in the background files and in the direction of AS1063. Therefore, we estimate that we can model the background at the ∼5% level. We assessed the impact of this background uncertainty by performing the temperature fits after scaling the background by ±5%. The fits were consistent with what we report with an rms < 5% for the regions with many cluster counts (from regions 1 to 7). In the last two regions, the fitted temperatures were different by as much as 10%. We also used background counts extracted from regions with negligible cluster emission. The fits were again consistent with what we report with an rms < 10%.

We fitted the Galactic absorption in two concentric annular regions. The first region is an annulus that has a 70 kpc inner radius and 200 kpc outer radius. We compute a value of $N_{\rm H} = (2.12 \pm 0.9) \times 10^{20}$ cm$^{-2}$ for the Galactic absorption in this region. The second annulus has an inner radius of 200 kpc and an outer radius of 400 kpc and we found a larger value of $N_{\rm H} = (3.8 \pm 1.4) \times 10^{20}$ cm$^{-2}$. Both estimates are higher than the radio value of $1.81 \times 10^{20}$ cm$^{-2}$ reported by Dickey & Lockman and the value of $1.23 \times 10^{20}$ cm$^{-2}$ reported by the Leiden/Argentine/Bonn (LAB) Survey of Galactic H I. Since we are uncertain as to the true galactic absorption toward this cluster and given the coarse resolution of the radio estimate, we decided to use our measured values for the spectral fits. The results are listed in Table 3 and plotted in Figure 15 with their 68% confidence errors for one parameter.

The cluster is very hot and does not show any evidence for a central cooling region. Moreover, taking into account the errors in the fits, the cluster appears to be isothermal out to an 800 kpc radius ($\sim r_{2500} \sim 3'$ see Figure 15) with a mean cluster temperature of $11.9^{+0.5}_{-0.6}$ keV for $N_{\rm H} = (3.8 \pm 1.4) \times 10^{20}$ cm$^{-2}$ and a temperature of $13.6^{+0.8}_{-0.9}$ keV for $N_{\rm H} = (2.1 \pm 1.4) \times 10^{20}$ cm$^{-2}$. Its average measured temperature within a smaller radius of 200 kpc is $12.3 \pm 0.8$ keV for the $N_{\rm H} = (3.8 \pm 1.4) \times 10^{20}$ cm$^{-2}$ case and can be as high as $14.3 \pm 0.7$ keV for the case of the lowest fitted $N_{\rm H}$. Maughan et al. (2008) reported a temperature of $11.1^{+0.8}_{-0.9}$ keV out to a radius of 6.′8. This is not surprising because they assumed a different cluster redshift. The metallicity shows the usual rise within the core that has been observed in other clusters (e.g., Vikhlinin et al. 2005) and drops to the typical average value of 0.3 solar at a radius of 130 kpc. Maughan et al. (2008) also show a metallicity gradient in their analysis. This is interesting and suggests that the core of the cluster has not been disturbed, as would be expected by a more extreme merger, i.e., a 1:2 or a 1:1 mass ratio event.

### *3.3.1. Modeling the Intracluster Medium*

In order to parameterize the spatial properties of the X-ray emission, we searched for the best-fit intracluster medium (ICM) model by simulating *Chandra* maps from an underlying 3D gas density distribution. The 3D distribution assumes a triaxial $\beta$-model (Cavaliere & Fusco-Femiano 1976) that is allowed to rotate about all three axes:

$$n_{\rm e}(r) = n_{\rm e0} \left(1 + \left(\frac{r}{r_{\rm c}}\right)^2\right)^{-\frac{3}{2}\beta}, \quad (3)$$

where $n_{\rm e0}$ is the central electron number density and $r_{\rm c}$ is the core radius. A triaxial model has a different core radius along each axis:

$$\left(\frac{r}{r_{\rm c}}\right)^2 = \left(\frac{r_x}{r_{cx}}\right)^2 + \left(\frac{r_y}{r_{cy}}\right)^2 + \left(\frac{r_z}{r_{cz}}\right)^2. \quad (4)$$

However, throughout the analysis presented in this paper we used a prolate model (unless specified), where we fixed the core

radius along the line of sight, $r_{cz}$, to be equal to the smallest of the other two core radii. We also limited rotation of the model to the plane of the sky.

The X-ray spectral surface brightness $b_X(E)$ along a given line of sight is

$$b_X(E) = \frac{1}{4\pi(1+z)^4} \int n_e(\mathbf{r})^2 \Lambda_c(E, T_e) dl, \quad (5)$$

where $n_e(\mathbf{r})$ is the electron number density as a function of distance $\mathbf{r}$ from the cluster center, $\Lambda_c(E, T_e)$ is the X-ray cooling function of the cluster gas (with electron temperature $T_e$) integrated over the energy band $E$. We used an isothermal temperature profile, as justified by Figure 15 and applied a cutoff to the 3D density profile at 15 core radii. This cutoff is motivated by two main reasons. First, it provides computational efficiency by limiting the fitting volume. Second, this cutoff radius is reasonable close to the virial radius (Eke et al. 1998 showed that $r_{virial} \sim 20 \times r_c$).

We calculated the cooling functions, $\Lambda_c$ (see the Appendix), required for our analysis in a pseudobolometric band [0.01,100] keV using XSPEC and the MEKAL model. For this we created a dummy response matrix with the range of [0.01,100.0] keV in 10,000 linearly divided steps. Next fake cluster spectra were generated in the [9.3 keV $< T_X <$ 16.3 keV] range with step size of 0.001 keV. For this, the metal abundance and redshift were fixed at $Z = 0.3\, Z_\odot$ and $z = 0$, respectively. From these spectra we created a grid of $\Lambda_c(T, Z)$ values for the range of possible temperatures for AS1063. These gridded values were then called on during our maximum likelihood analysis. Typical values for the cooling function are of order $10^{-23}$ (erg cm$^{-3}$ s$^{-1}$).

The ICM model fitting algorithm creates maps of the X-ray flux from Equation (5), by numerically integrating the model density profile, and then convolves the flux maps with instrument filters to simulate the signal from the *Chandra*/ACIS-I. These filters include beam smoothing with a model for the instrument beam (a Gaussian of FWHM of $\sim 2\farcs5$[13]), conversion from X-ray flux to photon count rate per pixel using an energy conversion factor (ECF; see the Appendix), and multiplication by the exposure map to obtain the total count per pixel. A constant background is then added to the simulated maps. A mask is applied during fitting such that only pixels with non-zero exposure time are considered.

The best-fit parameters for the model are determined by maximizing the likelihood estimator. The parameter adjustments are governed by a downhill simplex routine (Amoeba[14]). Assuming Poisson statistics, the log-likelihood of a simulated X-ray map is

$$\ln \mathcal{L}_X = \sum_i -\ln(N_{obs}(i)!) + N_{obs}(i)\, \ln(N_{sim}(i)) - N_{sim}(i), \quad (6)$$

where $N_{obs}(i)$ is the measured photon count for the $i$th pixel and $N_{sim}(i)$ is the simulated count. When we wish to account for uncertainties in the cluster temperature during a fit, we also include the following additional terms in the log-likelihood:

$$\ln \mathcal{L}_T = -\frac{1}{2}\left( \ln\left(2\pi\sigma_T^2\right) - \frac{(T_{sim} - T_{obs})^2}{\sigma_T^2} \right), \quad (7)$$

where $T_{sim}$ is the simulation input temperature and $T_{obs}$ is the independently observed temperature with an error of $\sigma_T$.

The first trial was a simple spherically symmetric beta model in which we allowed only $r_c$, $\beta$, $n_{e0}$, and the coordinates of the cluster center to vary. We applied the fit to the entire cluster, with no additional masking. For the second trial we added parameters to the model to allow for two core radii, $r_{c,x}$ and $r_{c,y}$, and a rotation in the plane of the sky. For this model type we then tried two different masks over the cluster core: a circular mask 18″ in radius (Trial 3) and an elliptical mask (Trial 4), defined using the best-fit core radii from Trial 2. The 18″ circular mask was an initial guess at the core radius. In Trial 5 we masked only a 4″ region around the central galaxy (roughly twice the point-spread function FWHM), to take into account a possible unresolved active galactic nucleus (AGN). We then added a second triaxial prolate beta model to the density profile and tested this both with and without masking of the central galaxy (Trials 6 and 7). We also attempted to model the substructure as an extra Gaussian component to the X-ray emission (Trials 8 and 9) to mimic a possible cool core or an AGN. The Gaussian component was not considered part of the underlying density distribution, but was an elliptical Gaussian added to simulated images of X-ray flux, before beam smoothing.

For all of these fitting trials we initially fixed the temperature of the system at 12.5 keV (which is reasonable average given the uncertainty in the Galactic absorption) and assumed a fixed flat background of 0.359 photons pixel$^{-1}$. We estimated this background level by measuring the average number of counts per pixel in four apertures, placed randomly around the X-ray image, avoiding the cluster, but spanning a good range of radii (from 6 to 8 arcmin).

In order to determine the type of model which provides the best overall fit, we subtracted each model from the original map and calculated the mean and standard deviation of the central region of the residual maps. The central region was defined as a $2' \times 2'$ box enclosing the cluster core. The residual maps are shown in Figure 16 and the statistics of the residuals of different model types in Table 4. Model 5 provides the best fit (i.e., small mean and standard deviation within a $2'$ region) of all the single component models considered. The best overall fit was obtained by modeling the cluster X-ray emission with a double beta model (Trials 6 and 7). A very slightly worse fit was obtained after masking the central cluster galaxy. However, we used this masking in all further analysis, since we felt it was better to account for any possible emission from a central AGN. Note that the double beta models are made of non-concentric beta models. The distance between the two beta-model centers is 21.″4 or ∼100 kpc at the redshift of the cluster. This is the underlying cause for the isophotal twisting described in Section 3.3.1.

We then repeated the double beta-model fit (Trial 7) for the two galactic absorption levels. For these fits, we also allowed the cluster temperature and the overall X-ray background level to vary as additional free parameters. Since the cluster appears quite isothermal and we did not have separate temperature measurements for the two model components, we assumed a single temperature for the entire system. The likelihood of this cluster temperature was included in the likelihood calculation, so that we could incorporate this source of uncertainty into the derived errors for the other parameters. The best-fit model parameters presented in Table 5 are for a temperature $T_e$ = 12.5 keV and errors are statistical only.

Once the best-fit parameters had been determined, we estimated the 68% confidence limits for each parameter using the

[13] 90% of the encircled energy lies within 5 pixels or 2.5 arcsec at 6.4 keV according to the "The *Chandra* Proposers' Observatory Guide."
[14] IDL routine based on *amoeba* from Press et al. (1992).

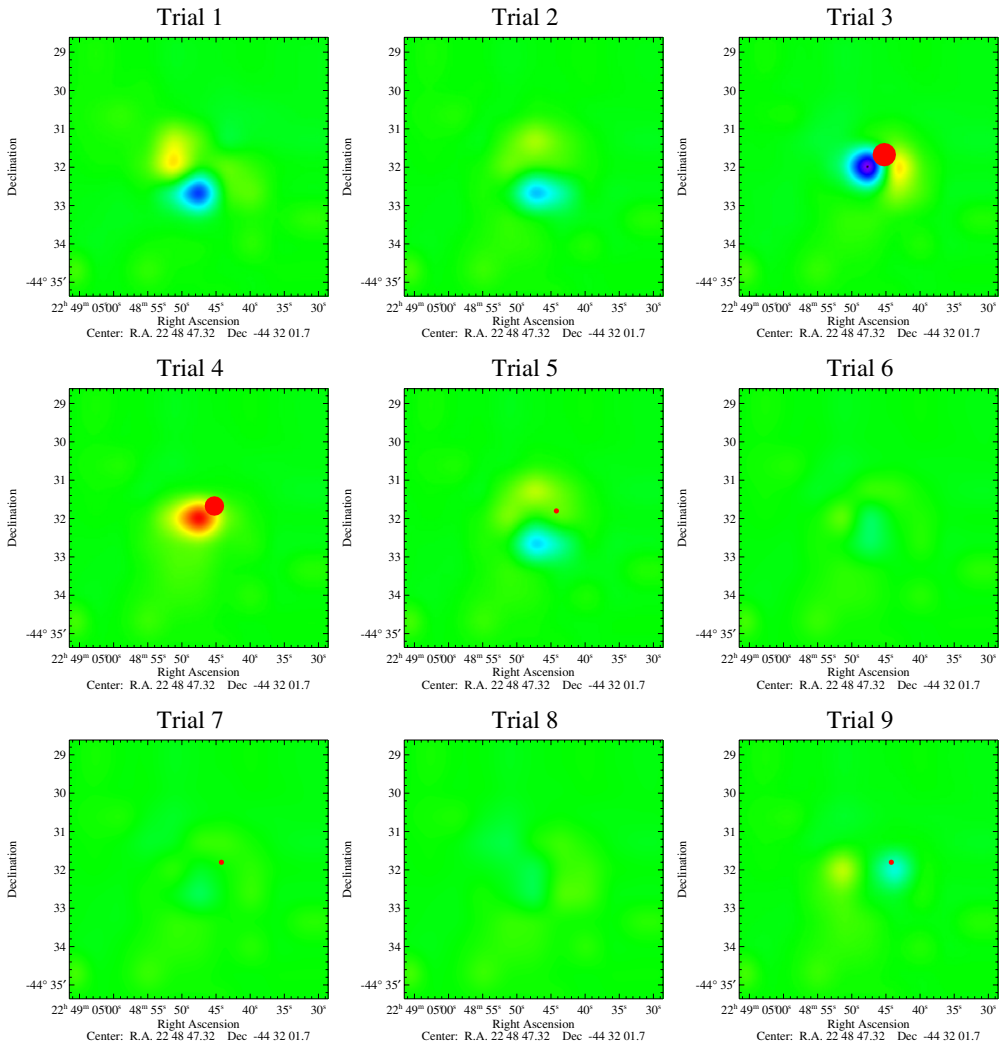


**Figure 16.** Residuals from the morphological fits. Each panel corresponds to one of the models depicted in Table 4. Please note that all the panels have been normalized to the same levels and have the same color palette. We also show in red the masked regions.

**Table 4**
A Comparison of Model Types Used for Fitting to the *Chandra* X-Ray Images, Listing the Mean and Standard Deviation of the Central Region ($2' \times 2'$) of the Residual Maps

| Trial | Model Components | Masking Used | Residual Map | |
|---|---|---|---|---|
| | | | Mean | st.dev. |
| 1 | Spherical single beta model | None | 0.04 | 9.08 |
| 2 | Elliptical single beta model | None | −0.23 | 7.76 |
| 3 | Elliptical single beta model | Circular region, radius 18 arcsec | −0.7 | 10.83 |
| 4 | Elliptical single beta model | Elliptical region, major axis 15 arcsec | 1.85 | 9.20 |
| 5 | Elliptical single beta model | Circular region around galaxy, radius 4 arcsec | 0.08 | 7.66 |
| 6 | Double beta model | None | −0.02 | 5.36 |
| 7 | Double beta model | Circular region around galaxy, radius 4 arcsec | −0.03 | 5.36 |
| 8 | Single beta model and Gaussian | None | −0.11 | 5.37 |
| 9 | Single beta model and Gaussian | Circular region around galaxy, radius 4 arcsec | −0.16 | 6.26 |

likelihood ratio test. The variable $S \equiv -2 \ln \mathcal{L}$ has a minimum value $S_{\rm min}$ for the best-fit parameters and therefore the Cash statistic (Cash 1979), $C = S - S_{\rm min}$, has a value of zero for the best-fit parameters and is greater than zero for any other parameter set. The 68% confidence region for a given parameter can be found by estimating the range of values for which the Cash statistic is less than unity. For each parameter in turn, the parameter was first fixed at an estimated point ($p - dp$) below the best-fit value ($p$) and a likelihood maximization performed marginalizing over the remaining free parameters and the Cash statistic evaluated for this fit. If $C$ was less than one, $dp$ was doubled and the marginalization repeated until a value of $C > 1$ was found. A cubic spline interpolation was then performed to estimate the $C = 1$ point and the Cash statistic again evaluated for this point. We carried out the interpolation four times and repeated the whole process for values above the best fit. This

**Table 5**
Best-fit Spatial Parameters for Isothermal Beta-model Fits to *Chandra* X-Ray Image

| | Trial 2<br>Single beta model, no masking | Trial 7<br>Double beta model, central galaxy masked |
|---|---|---|
| Component 1 | | |
| $r_c$(kpc)[a] | $151^{+1.2}_{-1.3}$, $120^{+1.2}_{-0.8}$ | $167.4^{+1.9}_{-0.8}$, $139.8^{+1.1}_{-1.5}$ |
| $\beta$ | $0.701^{+0.004}_{-0.003}$ | $0.674^{+0.007}_{-0.005}$ |
| $\phi$ (degrees counterclockwise) | $58.11^{+0.92}_{-0.90}$ | $54.51^{+1.58}_{-0.90}$ |
| R.A. | 22 48 $45.0^{+0.3}_{-0.1}$ | 22 48 $45.0^{+0.1}_{-0.1}$ |
| Decl. | −44 31 $43.1^{+0.1}_{-2.6}$ | −44 31 $43.2^{+0.1}_{-2.0}$ |
| Component 2 | | |
| $r_c$(kpc)[a] | ... | $98.7^{+0.7}_{-0.5}$, $61.7^{+0.5}_{-0.3}$ |
| $\beta$ | ... | $0.884^{+0.07}_{-0.04}$ |
| $\phi$ (degrees counterclockwise) | ... | $75.40^{+3.58}_{-3.37}$ |
| R.A. | ... | 22 48 $43.5^{+0.1}_{+0.1}$ |
| Decl. | ... | −44 31 $52.7^{+0.7}_{-2.0}$ |

**Notes.** Errors are statistical and we have assumed $h = 0.75$.
[a] Core radii in the plane of the image. The model is prolate, so the core radius along the line of sight is equal to the smallest of these.

**Table 6**
Best-fit Parameters

| Parameter | First Value | Second Value |
|---|---|---|
| $N_H(\times 10^{20}\,cm^{-2})$ | 2.1 | 3.8 |
| $n_{e0}(\times 10^{-2}\,cm^3)$ | $1.89^{+0.02}_{-0.04}$ | 1.90 |
| ... | $(3.31^{+0.1}_{-0.1})$ | (3.31) |
| $L_X(10^{44}\,erg\,s^{-1})$ | $87.8^{+4.5}_{-7.2}$ | 83.4 |
| $N_e(\times 10^{71})$ | $3.13^{+0.11}_{-0.17}$ | 3.17 |

**Note.** Central densities are given for both components of the best-fit double beta model with the value for the second component below the first (parenthesis).

method was first introduced by Cantalupo et al. (2002) and requires the sampling of relatively few points in the parameter space before the $C = 1$ points are found, as shown in Figure 17.

To quantify the error on the derived central electron density arising from the uncertainty in $n_H$, we fixed the best-fit shape parameters and fit for the central density using the two different $n_H$ estimates. The results are presented in Table 6.

We also wanted to quantify the possible systematic error arising from the assumed prolateness of the density profile. We found a 10% (20%) lower central density for the main (second) model component when using an oblate model instead of the prolate one. The decrease in central density is to be expected, since the oblate model in this case has a larger volume. Since the ellipticity of the second component is larger than that of the first, the effect of changing to the oblate model would also be expected to be larger in the second component, as we found. The best-fit oblate model had the same luminosity as the prolate model, since this is dictated by the observed flux, but the total number of electrons contained in the model was 9% higher.

### 3.3.2. Mass Calculation

The X-ray data can also be used to estimate the total cluster mass. First, we use the mass–temperature scale relation from Vikhlinin et al. (2006):

$$M_{2500} = \frac{M_5}{h(z)}\left(\frac{T}{5}\right)^{\alpha}, \quad (8)$$

where $M_{2500}$ is the mass within a radius where the overdensity is 2500 the critical density, $T$ is the average cluster temperature in keV, and $M_5$ is the normalization factor and is equal to $(1.25 \pm 0.05) \times 10^{14}\,M_\odot$. Thus, we obtained an $M_{2500} = (0.58 \pm 0.15) \times 10^{15}\,M_\odot$. We can further scale this value to $M_{200}$ and obtained a value of $M_{200} = (2.46 \pm 0.31) \times 10^{15}\,M_\odot$ by applying a conversion of $M_{200} = 4.27 \times M_{2500}$ derived from the scaling relations. For this we used the conservative estimate of $11.9 \pm 0.5$ keV for the average cluster temperature computed within $r_{2500} = 715$ kpc.

We also used the overall morphological fit to the cluster X-ray emission allows us to estimate the total mass within the cluster at different radii. In order to do this, we have to assume that the gas is isothermal and in hydrostatic equilibrium with a density distribution that follows a circular single $\beta$-model (i.e., our model 1 with $r_c$(kpc) $= 135^{+1.3}_{-1.3}$ and $\beta = 0.69^{+0.003}_{-0.003}$ with $\mu = 0.59$) then the mass at any radius can be expressed by (see Evrard et al. 1996)

$$M(<r) = 1.13 \times 10^{14}\beta\frac{T_X}{\mathrm{keV}}\frac{r}{\mathrm{Mpc}}\frac{(r/r_c)^2}{1+(r/r_c)^2}\,M_\odot. \quad (9)$$

In this expression $r_c$ corresponds to the core radius in the $\beta$-model, $T_X$ is the isothermal X-ray temperature, and $\beta$ is the usual model parameter. As we have done earlier, we use a value of $11.9^{+0.5}_{-0.6}$ keV for the gas temperature. Note that we used this fit since it is more physically realistic than the two $\beta$-models even though it is not the best fit to the data. The results at two different radii are listed in Table 7. The mass at a radius of 110 kpc is significantly smaller than the mass derived from the strong lens analysis. This is not surprising if this is indeed a merging cluster. In this case, the underlying assumptions of isothermality and hydrostatic equilibrium are wrong. A better estimate for the cluster mass as a function of radius can be derived from the X-ray data if we do a detailed comparison between the data and detailed numerical simulations. This study is beyond the scope of this work.

## 4. DISCUSSION

Our analysis of recent X-ray and optical data suggests that AS1063 is undergoing a major merger event. This conclusion

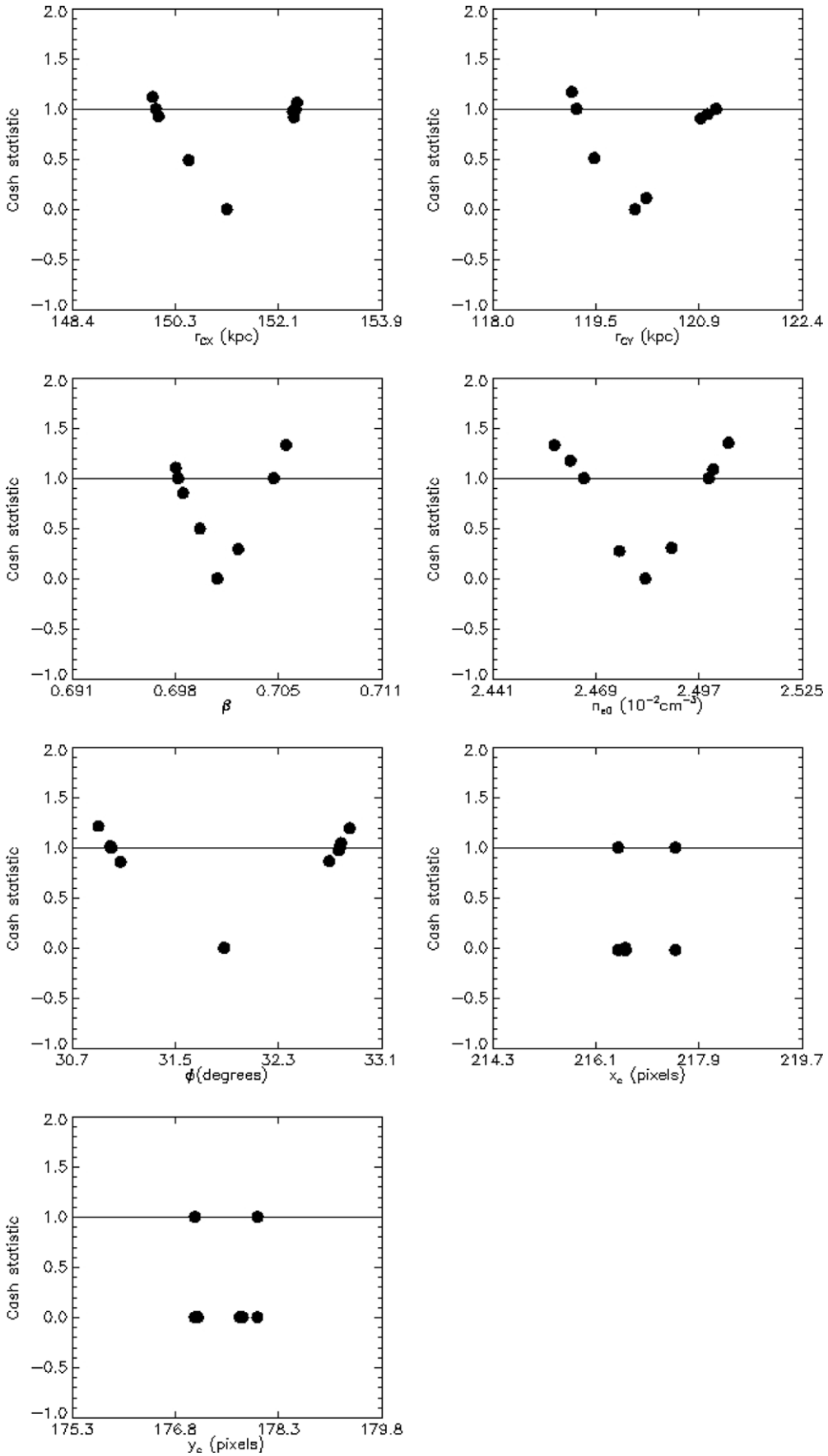


**Figure 17.** $1\sigma$ errors for each parameter are estimated by determining the range of parameter values for which the Cash statistic is $\leqslant 1$. The errors are plotted for each of the best-fit parameters for our single $\beta$-model fit. For each parameter, the points map out a Gaussian-like shape, except for the central coordinates $[x, y]$, for which the $1\sigma$ errors for the central coordinates are smaller than the pixel size of the image.

**Table 7**
Comparison of the Mass Estimations Based on the Analysis of the Data

| Method | Radius | Mass ($M_\odot$) | Assumptions |
|---|---|---|---|
| Optical (dynamical) | $r_{200}$ | $3.97^{+1.6}_{-0.9} \times 10^{15}$ | Depends on the velocity dispersion |
| X-ray data | $r_{200}$ | $2.46 \pm 0.31 \times 10^{15}$ | Depends on average temperature |
| X-ray data | 110 kpc | $6.1 \pm 0.1 \times 10^{13}$ | Isothermal, hydrostatic equilibrium, and spherical model |
| Strong lens | 110 kpc | $16.7 \pm 0.2 \times 10^{13}$ | Based on one background redshift |

is based on uncovering substructure in the distribution of the cluster galaxies and the distribution of the X-ray emitting gas consistent with a merger model. For instance, we found that a 1:4 mass ratio merger close to the epoch of core crossing provides a better match to the spatial and kinematical distribution of the galaxies than a relaxed cluster model. Furthermore, we have modeled the distribution of the X-ray emitting gas and found that the best fits are provided by non-concentric bimodal distributions and not by simple one-component models. These offset beta models (by as much as 21.″4) are the underlying cause for the X-ray elongation and isophotal twisting.

If we compare the distribution of X-ray emitting gas with the distribution of galaxy members (Figure 7) and likely cluster members (Figure 8), we uncovered a very interesting offset. As mentioned earlier, the distribution of the galaxy members is bimodal. Surprisingly, the X-ray peak emission is not centered on either galaxy peak. The offset is $37'' \pm 9''$ (or 170 kpc) between the X-ray centroid (see the previous section) and the nearest overdensity of galaxies (Figure 8). The offset is even larger if we compare the X-ray emission with the distribution of spectroscopically confirmed galaxies (offset of $57'' \pm 9''$ or 260 kpc). Moreover, the inner X-ray isophotes are elliptical and their major axis is roughly aligned with the two main galaxy density peaks (see Figure 9). The lens model also predicts an elongated total mass distribution with an angle of $63^\circ \pm 7^\circ$, which is similar to the galaxy clump orientation of 51.°3 and the X-ray elongation of $\sim 60^\circ$–$70^\circ$. This alignment is not perfect due to the fact that the X-ray isophotes change their position angle.

If we assume that the galaxies can be used to trace the dark matter potential, then the offset between the galaxies and the X-ray peaks is a typical signature of a recent cluster merger as seen on 1E0657-56, or the so-called bullet cluster (Markevitch 2006; Markevitch et al. 2002). Numerical simulations of cluster mergers have shown that when the cores interact, the gas is not in hydrostatic equilibrium with the gravitational potential and appears elongated (e.g., Roettiger et al. 1997; Gómez et al. 2002; Poole et al. 2006). Depending on the type or merger (i.e., mass ratio between the interacting clusters, baryon fraction in each), the displacement can last up to a few gigayears after core crossing. As could be expected, this effect is easily seen in mergers happening close to the plane of the sky. As it turns out, these are the types of mergers that are more difficult to diagnose based on the galaxy kinematics. This perhaps explains why we do not see strong evidence for a merger from the optical data.

The merger model could also explain the large mass estimate for the cluster derived from the X-ray and the optical data. If the cluster is indeed undergoing a merger similar to the 1:4 mass ratio merger seen 0.5 Gyr after core crossing, then we could have a case in which the actual mass of the main cluster is lower, i.e., $\simeq 1.5 \times 10^{15}\ M_\odot$ (Section 2.3.5). The mass estimates derived from these data would be larger than the actual value because they assume that the cluster follows the scaling relations. It would be interesting to calculate the mass of the whole cluster independent of the assumption of isothermality and virialization by combining strong-lens and future weak-lensing analysis.

Figure 15 shows that AS1063 is roughly isothermal. By comparison, Vikhlinin et al. (2005) have analyzed the temperature profile for a sample of nearby relaxed clusters. They found that these clusters are characterized by a cool core and a temperature profile that is slowly rising to a maximum at a radius $\sim 0.15 \times r_{180}$ and then it drops to half the peak temperature at $0.5 \times r_{180}$ (where $r_{180} = 1.88$ Mpc $(\langle T \rangle / 10\ \mathrm{keV})^{1/2}$). The absence of a cooling core in AS1063 is further suggestive that the cluster is not as relaxed as the ones observed by Vikhlinin et al. (2005).

The conclusions drawn from the "bullet cluster" (i.e., 1E0657-56) that the X-ray derived mass estimates are too high because the merger has boosted the X-ray temperature (see Section 1) might well apply to AS1063 also. The two clusters have similar X-ray temperatures (14.3 keV for AS1063 versus 14.1 keV for 1E0657-56; Markevitch et al. 2002) and have mergers of similar mass ratios (a possible 1:4 for AS1063 versus 1:6 for 1E0657-56; Mastropietro & Burkert 2008) and orientations on the sky. Gas shocks produced in the ICM during this merger would also explain the flat temperature profile measured in this cluster given our coarse radial binning. Under this scenario, the gas would be expected to settle down into a more stable gravitational potential within a few gigayears. This would also result in the emergence of a more typical X-ray temperature profile, i.e., one that rises and then falls with increasing radius (Vikhlinin et al. 2006).

There are differences between 1E0657-56 and AS1063, however. AS1063 shows no evidence for a "cold bullet," whereas 1E0657-56 does not show the twisted X-ray isophotes. We note that other clusters with reported isophotal twisting include A665 (Gómez et al. 2000) and A3266 (Flores et al. 2000). A3266 has been modeled in detail as a non-axis merger observed some 3 Gyr after core crossing and with a mass ratio of 2.5:1 (Roettiger & Flores 2000).

## 5. CONCLUSIONS

In this paper, we present the results of recent optical and X-ray observations of AS1063. These observations were obtained to improve our previously limited knowledge of the properties of this cluster. Our analysis of the data has shown that AS1063 has a similar redshift and X-ray temperature to the well-known "bullet cluster." We have also uncovered evidence that AS1063 is undergoing a major merger in the plane of the sky.

The analysis of archival ESO NTT and GMOS direct images have uncovered a cluster with a well-defined red sequence. We also determined that there is substructure and bimodality in the spatial distribution of the galaxies. Moreover, we discovered the presence of several gravitational arc candidates close to the cluster core. We measured the redshift for 51 galaxy cluster members that yielded a cluster redshift of $z = 0.346$ and measured the redshift of one of the gravitational arcs at

$z = 0.61$. We have also compared the observed velocity and spatial distribution of the galaxies with simple *N*-body numerical simulations. We find that 1:4 mass ratio mergers observed between 0.5 and 1 Gyr and with viewing angles between 80° and 90° have a 90% probability of having the same parent velocity distribution as the observed distribution and similar spatial bimodality.

The *Chandra* X-ray observations revealed a very hot intracluster gas with a temperature of up to ∼14.3 keV. The temperature profile is fairly flat and extends out to 350 kpc. Moreover, the twisted and off-center isophotes reveal substructure in the spatial distribution of the X-ray emitting gas. Furthermore, the central region of the cluster is complex and can be better modeled by two non-concentric $\beta$-models than by a single or even a double concentric $\beta$-model.

The peak of the X-ray emission does not coincide with any peak of the galaxy distribution. The closest galaxy peak is located at 37″ (170 kpc) from the X-ray peak. Furthermore, the inner X-ray isophotes are elongated parallel to the direction that joins the two main galaxy density peaks and the elongation of the dark matter distribution predicted by the lens model. If we assume that the galaxies traced the dark matter potential, then we could explain the substructure found in the X-ray gas, the offset between the gas and the galaxies, and the alignment between the X-ray and the galaxy distribution elongations. These are the tell tale signs of a merger stage at which the intracluster gas is trying to regain hydrostatic equilibrium with a changing gravitational potential. As a result the cluster gas could have a large temperature produced by shocks and its distribution has not been able to settle down yet.

These data also allowed us to estimate the mass of the cluster by making several key assumptions. We have used the $M_{200}$–$\sigma_{\rm DM}$ scaling relation from Evrard et al. (2008) to estimate an $M_{200} = (3.97 \pm 0.8) \times 10^{15}\ M_{\odot}$. The gravitational arc provides another estimate of $M(r < 25'') = (1.66 \pm 0.08) \times 10^{14}\ M_{\odot}$. Finally, we have used the X-ray temperature and the mass–temperature scale relation from Vikhlinin et al. (2006) to derive an $M_{200} = (2.46 \pm 0.31) \times 10^{15}\ M_{\odot}$.

We propose that AS1063 has undergone a recent merger close to the plane of the sky similar to the one experienced by the "bullet cluster" and by A3266. The AS1063 merger is probably slightly off-axis since there is X-ray isophotal twisting (compare with the simulations by Ricker & Sarazin 2001). This type of off-axis merger in the plane of the sky would explain the misalignment between the X-ray emitting gas and the galaxies, the twisted isophotes, the apparent lack of non-Gaussianity in the distribution of the galaxy velocities, and the high temperature and high X-ray luminosity. Future studies will compare in more detailed numerical simulations of cluster mergers with the optical (including lensing data) and X-ray data for this cluster in order to further understand and identify the merger in this system.

This research was possible with financial support from: (1) NASA (via the *XMM* and *Chandra* Guest Observer programs and the Long Term Space Astrophysics program, grant Nos. NAG5-7926, NAG5-12999, NAG5-20453, GO4-5141X); (2) the European Commission (via a Marie Curie Reintegration Grant, grant number EIF-OIF-IIF-IRG-ERG; Project 513676); (3) AAS (via international travel grants for 2003 and 2004 and a small research grant); (4) STFC (the UK Science and Technology Facilities Council) (K.R., P.G.); (5) the Osk. Huttunen Foundation for a PhD studentship (L.V.); (6) the Magnus Ehrnrooth Foundation for a travel grant (L.V.); and (7) the University of Sussex Physics and Astronomy Department for a Graduate Teaching Assistantship (L.V.). In addition P.L.G. thanks the kindness of the Sussex Astronomy Centre during month long visits in 2006 and 2007. P.L.G. also thanks the European Southern Observatory (ESO) for two short stays at their Headquarters in Santiago where a large fraction of the final version of this paper was written. Finally, we thank the referees for helping us write a more concise, accurate, and hopefully interesting paper.

This work is based on observations obtained from (1) the Gemini Observatory, which is operated by the Association of Universities for Research in Astronomy, Inc., under a cooperative agreement with the NSF on behalf of the Gemini partnership: the National Science Foundation (United States), the Science and Technology Facilities Council (United Kingdom), the National Research Council (Canada), CONICYT (Chile), the Australian Research Council (Australia), Ministrio da Cincia e Tecnologia (Brazil), and SECYT (Argentina); (2) the *Chandra X-Ray Observatory* (*Chandra*) is operated by the Smithsonian Astrophysical Observatory for and on behalf of the National Aeronautics Space Administration under contract NAS8-03060; and (3) the ESO telescopes at La Silla under program 70.A-0074.

## APPENDIX

## X-RAY COOLING FUNCTIONS AND ENERGY CONVERSION FACTORS

For reasons of completeness, we include here some background to explain X-ray cooling functions. For a typical cluster ($kT \geqslant 2$ keV) the emissivity of thermal bremsstrahlung continuum dominates that from emission lines and the cooling function can be approximated by $\Lambda \propto T^{1/2}$. The luminosity per unit volume is defined either as $n_e n_{\rm H} \Lambda_c(T, Z)$ or $n_e n_{\rm ion} \Lambda_c(T, Z)$, such that $\Lambda_c(T, Z)$ is the corresponding cooling function. For typical ICM temperatures and abundances, $\Lambda_c \sim 10^{-23}$ erg cm$^3$ s$^{-1}$ (Voit 2005).

The differential flux $F_\nu$ is related to the differential luminosity $L_\nu$ via the following relation:

$$F_\nu = (1+z)\frac{L_{(1+z)\nu}}{4\pi D_L^2}, \tag{A1}$$

where $D_L = D_A(1+z)^2$ is the luminosity distance to the source and

$$L_\nu = \int n_e n_{\rm H} \Lambda_\nu(T, Z)\, dV. \tag{A2}$$

Many codes exist to compute $\Lambda_c(T, Z)$ such as Raymond–Smith (Raymond & Smith 1977) and MEKAL (Mewe et al. 1985). The normalization $N$ of the spectrum in both MEKAL and Raymond–Smith models in XSPEC is

$$N = \frac{10^{-14}}{4\pi[D_A(1+z)]^2} \int n_e n_{\rm H}\, dV, \tag{A3}$$

where $D_A$ is the angular diameter distance to the source (cm), and $n_e$, $n_{\rm H}$ (cm$^{-3}$) are the electron and hydrogen density (with a net dimension of cm$^{-5}$). Since they share this form, the flux to temperature estimations will only be affected thorough cooling function variations.

Using Equations (A3), (A1), and (A2) with the assumption of isothermal gas with uniform metallicity, it is easy to show that

$$\Lambda_{c^*}(T, Z) \equiv \int_{\nu_0(1+z)}^{\nu_1(1+z)} \Lambda_\nu\, d\nu = \frac{(1+z)^2 F_{h[\nu_0,\nu_1]}}{N} * 10^{-14}, \tag{A4}$$

where $\Lambda_c(T, Z)$ is the cooling function integrated in the emitted frequency band of $[\nu_0(1+z), \nu_1(1+z)]$ in the rest frame of the source, which is observed in the $[\nu_0, \nu_1]$ frequency interval due to cosmological redshift.

In addition to using cooling functions, we have also used ECFs during our cluster fitting. These convert count rates to energy fluxes (and vice versa). These ECFs effectively encode the energy-dependent sensitivity of the instruments convolved with the spectrum of the source under study. For clusters, the spectral properties are a function of the cluster redshift, the plasma temperature, the metal enrichment in the intracluster gas and the absorbing column along the line of sight. Therefore, to generate ECFs appropriate for this cluster at $z = 0.3461$, we created 24,000 fake (absorbed) MEKAL spectra using XSPEC on an $T$ and $n_{\rm H}$ grid such that [min, max, step] were [1, 12, 1] and [0.01, 0.50, 0.01], respectively. For this, we assumed that the abundance is 0.3 solar and the spectral normalization is 1.

## REFERENCES


Abell, G. O., Corwin, H. G., Jr., & Olowin, R. P. 1989, ApJS, 70, 1
Beers, T. C., Flynn, K., & Gebhardt, K. 1990, AJ, 100, 32
Bertin, E., & Arnouts, S. 1996, A&AS, 117, 393
Binney, J., & Tremaine, S. (ed.) 2008, Galactic Dynamics (2nd ed.; Princeton, NJ: Princeton Univ. Press)
Böhringer, H., Schuecker, P., Guzzo, L., et al. 2004, A&A, 425, 367
Cantalupo, C. M., Romer, A. K., Peterson, J. B., et al. 2002, arXiv: astro-ph/0212394
Cash, W. 1979, ApJ, 228, 939
Cavaliere, A., & Fusco-Femiano, R. 1976, A&A, 49, 137
Cruddace, R., Voges, W., Bhringer, H., et al. 2002, ApJS, 140, 239
Danese, L., de Zotti, G., & di Tullio, G. 1980, A&A, 82, 322
D'Odorico, S., Beletic, J. W., Amico, P., et al. 1998, Proc. SPIE, 3355, 507
Dressler, A., & Shectman, S. A. 1988, AJ, 95, 985
Eke, V. R., Navarro, J. F., & Frenk, C. S. 1998, ApJ, 503, 569
Elíasdóttir, Á., Limousin, M., Richard, J., et al. 2007, arXiv:0710.5636
Evrard, A. E., Bialek, J., Busha, M., et al. 2008, ApJ, 672, 122
Evrard, A. E., Metzler, C. A., & Navarro, J. F. 1996, ApJ, 469, 494
Fitchett, M., & Webster, R. 1987, ApJ, 317, 653
Flores, R. A., Quintana, H., & Way, M. J. 2000, ApJ, 532, 206
Gómez, P. L., Hughes, J. P., & Birkinshaw, M. 2000, ApJ, 540, 726
Gómez, P. L., Loken, C., Roettiger, K., & Burns, J. O. 2002, ApJ, 569, 122
Hook, I. M., Jørgensen, I., Allington-Smith, J. R., et al. 2004, PASP, 116, 425
Jedrzejewski, R. I. 1987, MNRAS, 226, 747
Jullo, E., Kneib, J.-P., Limousin, M., et al. 2007, New J. Phys., 9, 447
Lee, M. A. 1979, ApJ, 229, 424
Markevitch, M. 2006, in The X-ray Universe 2005, ed. A. Wilson (ESA SP-604; Spain: ESA), 723
Markevitch, M., Gonzalez, A. H., David, L., et al. 2002, ApJ, 567, L27
Markevitch, M., & Vikhlinin, A. 2007, Phys. Rep., 443, 1
Mastropietro, C., & Burkert, A. 2008, MNRAS, 389, 967
Maughan, B. J., Jones, C., Forman, W., & Van Speybroeck, L. 2008, ApJS, 174, 117
Mewe, R., Gronenschild, E. H. B. M., & van den Oord, G. H. J. 1985, A&AS, 62, 197
Mohr, J. J., Evrard, A. E., Fabricant, D. G., & Geller, M. J. 1995, ApJ, 447, 8
Mohr, J. J., Fabricant, D. G., & Geller, M. J. 1993, ApJ, 413, 492
Nagai, D., Kravtsov, A. V., & Vikhlinin, A. 2007, ApJ, 668, 1
Pinkney, J., Roettiger, K., Burns, J. O., & Bird, C. M. 1996, ApJS, 104, 1
Poole, G. B., Fardal, M. A., Babul, A., et al. 2006, MNRAS, 373, 881
Press, W. H., Teukolsky, S. A., Vetterling, W. T., & Flannery, B. P. 1992, Numerical Recipes in C: The Art of Scientific Computing (2nd ed.; Cambridge: Cambridge Univ. Press)
Raymond, J. C., & Smith, B. W. 1977, ApJS, 35, 419
Ricker, P. M., & Sarazin, C. L. 2001, ApJ, 561, 621
Roettiger, K., & Flores, R. 2000, ApJ, 538, 92
Roettiger, K., Loken, C., & Burns, J. O. 1997, ApJS, 109, 307
Smith, G. P., Kneib, J.-P., Smail, I., et al. 2005, MNRAS, 359, 417
Springel, V., & Farrar, G. R. 2007, MNRAS, 380, 911
Sunyaev, R. A., & Zel'dovich, Y. B. 1970, Ap&SS, 6, 358
Vikhlinin, A., Kravtsov, A., Forman, W., et al. 2006, ApJ, 640, 691
Vikhlinin, A., Markevitch, M., Murray, S. S., et al. 2005, ApJ, 628, 655
Voit, G. M. 2005, Rev. Mod. Phys., 77, 207
West, M. J., & Bothun, G. D. 1990, ApJ, 350, 36
West, M. J., Oemler, A. J., & Dekel, A. 1988, ApJ, 327, 1
White, M., Cohn, J. D., & Smit, R. 2010, MNRAS, 408, 1818
Yahil, A., & Vidal, N. V. 1977, ApJ, 214, 347